https://doi.org/10.5194/egusphere-2025-2258
Preprint. Discussion started: 28 May 2025

Global ocean and sea ice variability simulated in eddy-permitting climate models

Yushi Morioka[1], Eric Maisonnave[2], Sébastien Masson[2], Clement Rousset[2], Luis Kornblueh[3], Marco Giorgetta[3], Masami Nonaka[1], Swadhin K. Behera[1]

1: Application Laboratory, VAiG, JAMSTEC, Yokohama, Japan
2: LOCEAN-IPSL, Sorbonne Université, Paris, France
3: Max Planck Institute for Meteorology, Hamburg, Germany

May 14, 2025 (submitted)
Geoscientific Model Development

Corresponding Author: Yushi Morioka
Showamachi 3173-25, Kanazawa-ku, Yokohama, JAPAN
morioka@jamstec.go.jp, +81-45-778-5509

https://doi.org/10.5194/egusphere-2025-2258
Preprint. Discussion started: 28 May 2025

Abstract

Ocean mesoscale eddies, which have a horizontal scale with an order of 100 km, play a prominent role in global ocean heat transport that regulates the Earth's climate. Most of climate models, however, cannot fully resolve the ocean mesoscale eddies because of the constraint of computational resources. To mitigate this shortcoming, we newly develop an eddy-permitting climate model, SINTEX-F3, which has the ocean resolution with the order of 25 km. Compared to other eddy-permitting climate models available from the CMIP6 HighResMIP, the SINTEX-F3 represents a cold bias in the mid-high latitudes and weaker El Niño-Southern Oscillation (ENSO). Despite the weaker ENSO, the SINTEX-F3 realistically reproduces other tropical climate phenomena such as the Indian Ocean Dipole and Atlantic Niño/Niña, indicating that these modes are less dependent on ENSO in the model. In the subtropical-midlatitudes, the SINTEX-F3 well captures mesoscale sea surface temperature and surface heat flux variability, particularly in the western and eastern boundary current regions. Furthermore, the SINTEX-F3 simulates the mean state and variability of sea ice in the Antarctic Sea more accurately than in the Arctic Sea, likely due to improvements in sea ice model physics and the increased ocean model resolution. While further efforts are needed to address the cold bias and the weaker ENSO representation, the SINTEX-F3 shows significant potential for simulating and predicting global ocean and sea ice variability at an eddy-permitting scale.

https://doi.org/10.5194/egusphere-2025-2258
Preprint. Discussion started: 28 May 2025

1. Introduction

Ocean mesoscale eddies, which have a horizontal scale with the order of 100 km (Chelton et al., 2011) and a vertical scale with the order of 1 km (Zhang et al., 2013), contribute to global transport of momentum (Zhang et al., 2014), heat (Morrison et al., 2016), salinity/freshwater (Melnichenko et al., 2017), and dissolved gases (Munday et al., 2014) that regulate the Earth's climate. The mesoscale eddies are more energetic in the western boundary current regions and the Southern Ocean where the isopycnals steepen to increase the baroclinicity and the available potential energy (Griffies et al., 2015). In these regions, the mesoscale eddies transport heat upward in the process of releasing the available potential energy, partially offsetting the downward heat transport from the mean ocean circulation.

Many efforts have been made for understanding a role of ocean mesoscale eddies in the mean state of climate system, but less has been known about the impact of the mesoscale eddies on the climate variability over the global oceans. For example, in the eastern tropical Pacific (e.g., Willett et al., 2006), the ocean mesoscale eddies are generated through the latitudinal velocity shear between the westward South Equatorial Current and eastward North Equatorial Counter Current and Equatorial Undercurrent, and propagate westward as the tropical instability wave (TIW). The TIW is more active during La Niña due to a stronger meridional sea surface temperature (SST) gradient and baroclinic instability (Yu and Liu, 2003), which brings anomalous warming to cause a negative feedback. This leads to asymmetricity in the amplitudes of ENSO with stronger El Niña than La Niña (An, 2008). In the eastern tropical Indian Ocean, the large negative SST anomaly associated with the positive Indian Ocean Dipole (IOD), for example, in 1994, enhances the mesoscale eddy activity through the baroclinic instability and contributes to the decay through the eddy heat transport (Ogata and Masumoto, 2010), although only a little influence of the mesoscale eddies is found for the other case of the positive IOD in 1997. In the tropical Atlantic, most of the mesoscale eddies are located subsurface with their maximum temperature and salinity anomalies below the pycnocline, accompanied by the inverse SST anomalies (i.e., the cold SST anomalies for the anticyclonic eddies). A recent study (Aguedjou et al., 2023) suggests that the inverse eddy SST anomalies may impact both heat flux and precipitation in the Intertropical Convergence Zone (ITCZ). However, the role of the ocean mesoscale eddies in the tropical climate variability such as the Atlantic Niño/Niña has been poorly understood.

In the subtropical and midlatitude oceans, the western and eastern boundary currents involve more vigorous mesoscale eddies generated mainly through the baroclinic instability,

https://doi.org/10.5194/egusphere-2025-2258
Preprint. Discussion started: 28 May 2025

but the characteristics of the eddies and their impacts on the overlying atmosphere largely depend on the regions. In the Gulf Stream region, warm (anticyclonic) eddies form off the northward meander of the warm Sargasso Sea water, whereas cold (cyclonic) eddies spin off the southward meander and travel to the south into the Sargasso Sea (Auer, 1987). The warm eddies tend to increase the surface wind by deepening a marine boundary layer and vice versa, which leads to wind convergence and divergence across the eddies (Chelton et al., 2004). In the northwestern Pacific, the warm eddies pinch off from the Kuroshio Extension to the north, while the cold eddies form to the south from the troughs of the Kuroshio Extension (Itoh and Yasuda, 2010). Both warm and cold eddies propagate westward as oceanic Rossby waves affecting the strength of the Kuroshio Extension and recirculation gyre (Qiu and Chen, 2005). After reaching the Japan coast, the warm eddies tend to move poleward along the subarctic front and trenches (Itoh and Yasuda, 2010). These eddies transport the heat poleward across the Kuroshio Extension to counteract the oceanic heat loss from air-sea fluxes north of the Kuroshio Extension (Dong et al., 2017).

In the Southern Hemisphere, the confluence of the Malvinas Current and the Brazil Current shapes one of the most energetic regions over the global oceans. Warm eddies are generated south of the subtropical front through the poleward meander of the Brazil Current, whereas cold eddies tend to form north of the front (Saraceno and Provost, 2012). The warm eddies tend to increase the surface wind and the turbulent heat flux from the ocean to the atmosphere (Pezzi et al., 2021). In contrast to other western boundary current regions, the cold eddies tend to release more heat to the atmosphere (Leyba et al., 2017), because most of the cold eddies originate within the very warm subtropical water and propagate southward. In the Agulhas Current region, the warm eddies form at the retroflection region, and some of the eddies become Agulhas rings pinched off the Agulhas retroflection loop, losing heat to the atmosphere (Lutjeharms and Valentine, 1988). The warm eddies also form downstream at the Agulhas Plateau by intrusion of cold subantarctic surface water. The warm eddies tend to deepen the atmospheric boundary layer via the increased turbulent heat flux (Messager and Swart, 2016). However, it is worth noting that only a half of the warm eddies represents higher wind speed over the warm eddies (Rouault et al., 2016). In the East Australian Current, warm eddies form by pinch-off of poleward meander of the East Australian Current, but most eddies do not escape to the south but coalesce with the East Australian Current (Nilsson and Cresswell, 1981). The mesoscale variability arises from an intrinsic instability of the western boundary current, not from the remote mesoscale signals propagating westward from the South Pacific

https://doi.org/10.5194/egusphere-2025-2258
Preprint. Discussion started: 28 May 2025

(Bowen et al., 2005). However, the influence of these mesoscale variability onto the overlying atmosphere remains unclarified.

In contrast to the western boundary current regions, the ocean mesoscale eddies in the eastern boundary current regions are less studied but play important roles in the marine biological activities through changes in the coastal upwelling (Gruber et al., 2011). Most of the eddies arise from the baroclinic/barotropic instability of the inshore and offshore currents and contributes to the offshore cooling except within the 50-100 km from the shore (Capet et al., 2008). The eddies undergo distinct seasonal variations in the California upwelling region, and show large interannual variations in the Benguela and Canary upwelling regions (Chaigneau et al., 2009). However, the influence of the eddies on the coastal SST variability known as the coastal Niño/Niña (i.e., Benguela Niño/Niña, Shannon et al., 1986; Ningaloo Niño/Niña, Feng et al., 2013, Kataoka et al., 2014; California Niño/Niña, Yuan and Yamagata, 2014; Dakar Niño/Niña, Oettli et al., 2016; Chile Niño/Niña, Xue et al., 2020) has yet been studied.

In the polar regions, the role of ocean mesoscale eddies is more studied in the Arctic Sea than the Antarctic Sea. The Arctic eddy activity strengthens near the surface during boreal summer due to the absence of sea ice cover that prevents the baroclinic instability from occurring below the sea ice. The subsurface eddy activity, on the other hand, persists all year long within the deeper halocline and below (e.g., Manley and Hunkins, 1985), owing to the interior potential vorticity gradient constrained by the Atlantic and Pacific waters (Meneghello et al., 2021). As the Arctic sea ice declines, the surface eddy activity strengthens to bring more subsurface warm water to the surface and contributes to the sea ice decline (Manucharyan and Thompson, 2022; Li et al., 2024). The mesoscale eddies in the Antarctic Sea, on the other hand, are less studied probably due to shortage of the ocean observations. Using an eddy-resolving coupled model, Dufour et al., (2017) successfully simulated sea ice polynya events associated with ocean mesoscale eddies in the Weddell Sea. Resolving the mesoscale eddies and overflows of the dense continental shelf waters allow the subsurface ocean heat to build up and destratify the upper ocean thereby melting the sea ice from below. Cheon and Gordon (2019) also reported the role of ocean cyclonic eddies in the upwelling of warm Weddell Deep Water and the Maud Rise Polynya in 2017. Since the open-water polynya affects the turbulent heat flux, radiative flux, cloud, and precipitation locally (Weijer et al., 2017), it is imperative to resolve the ocean mesoscale eddies for better representation of the atmosphere-ocean-sea ice interaction in the polar regions.

However, it remains a big challenge to fully resolve the ocean mesoscale eddies from the tropics to the polar oceans in climate models with reasonable computational resources. This

https://doi.org/10.5194/egusphere-2025-2258
Preprint. Discussion started: 28 May 2025

is because nominally 1º resolution is sufficient for the ocean model to resolve the mesoscale eddies near the Equator, but in the subtropics and midlatitudes, much higher resolutions than 0.1º are required for resolving the mesoscale eddies on the continental shelfs and in the polar regions (Hallberg et al., 2013). Most of climate models used for recent climate research have the ocean resolutions of nominally 1/2º to 1º owing to the constraint of the computational resources. Therefore, most of the models cannot fully resolve the ocean mesoscale eddies but emulate the effect of eddies, for example, on lateral mixing by a simplified parameterization (Gent and McWilliams, 1990).

To address the resolution issues, the 6th phase of the Coupled Model Intercomparison Project (CMIP6) has recently launched the High Resolution Model Intercomparison Project (HighResMIP; Haarsma et al., 2016) where the eddy-permitting climate models with the ocean resolution of about 1/4º are developed for the comparison with the eddy-parameterized lower resolution models. For example, in the tropical Pacific, the spatial pattern of ENSO improves with the increased ocean model resolution, likely due to the improved mean state and associated surface thermodynamic feedback process (Liu et al., 2022). This also leads to better representation of the atmospheric teleconnection to the North Pacific (Williams et al., 2024). In the Gulf Stream region, the high-resolution coupled models tend to capture the simultaneous cross-covariance between the SST and turbulent heat flux, closer to the observation (Bellucci et al., 2021). In the Kuroshio region, however, only two high-resolution coupled models represent some improvement of the Kuroshio Extension intensity and enhanced warming trend in the past (An et al., 2023). In the polar regions, the increased ocean model resolution shows limited benefits in simulating the historical changes in the Antarctic sea ice (Selivanova et al., 2024a) compared to the Arctic sea ice (Selivanova et al., 2024b). These results indicate the pros and cons of the increased ocean model resolution and the need of further improvement of ocean and sea ice model physics as well as the model resolution.

Despite these previous findings, the role of ocean mesoscale eddies in the interannual climate variability have not been fully understood. Therefore, this study aims to address the following research questions: Can the eddy-permitting models better simulate the interannual climate variability over the global ocean and sea ice than the eddy-parameterized models? If so, what are possible reasons for the better representation of interannual climate variability in the eddy-permitting models? What are the remaining issues for the eddy-permitting models to better simulate the interannual climate variability? For this purpose, we develop an eddy-permitting climate model and compare the control simulations under the constant radiative forcing with those in the previously developed eddy-parameterized climate model and other

https://doi.org/10.5194/egusphere-2025-2258
Preprint. Discussion started: 28 May 2025

available climate models from the CMIP6 HighResMIP. This paper is organized as follows: In Sect. 2, we describe the observation data and reanalysis product, climate model configurations, and climate indicators. In Sect. 3, we compare the eddy-parameterized and eddy-permitting models for the climate variability in the tropics, western and eastern boundary current regions, and the polar regions. In Sect. 4, we discuss possible reasons for the mean state and variability biases in the eddy-permitting models. In Sect. 5, we conclude the main results and suggest future work on addressing the remaining issues.

2. Methodology

2.1. Observation data and reanalysis product

For comparison with climate model simulations, we used monthly high-resolution SST using the optimum interpolation version 2 (OI.v2) provided by NOAA (OISST2_hi; Reynolds et al., 2007). It has a 0.25º x 0.25º horizontal resolution over the analysis period of 1982-2022. We also used daily sea ice concentration (SIC) from Nimbus-7 SMMR and DMSP SSM/I-SSMIS passive microwave data, version 2 provided by NSIDC (NSIDC_Nimbus; DiGirolamo et al., 2022). The SIC data has the same horizontal resolution and period with the SST data. Furthermore, we used quality-controlled ocean potential temperature and salinity objective analyses with Gouretski and Reseghetti (2010) XBT corrections and Gouretski and Cheng (2020) XBT corrections provided by UK Met Office (EN4; Good et al., 2013). It has a 1º x 1º horizontal resolution with 31 vertical levels over the period of 1982-2022. For the atmospheric variables, we employed monthly sea level pressure (SLP), net surface heat flux, zona wind speed at 10 m, and shortwave and longwave radiations at the top of the atmosphere from the ERA5 reanalysis product (Hersbach et al., 2020). It has a 0.25º x 0.25º horizontal resolution over the period of 1982-2022.

2.2. SINTEX-F2 and SINTEX-F3 models

As a reference for the eddy-parameterized coupled model, we used the second version of the Scale Interaction Tropical Experiment-Frontier (SINTEX-F2; Masson et al., 2012, Sasaki et al., 2012) model. The oceanic component of the SINTEX-F2 is based on the Nucleus for European Modeling of the Ocean (NEMO3.4; Madec, 2008) system which comprises the Ocean Parallelise (OPA9) ocean model and the Louvain-la-Neuve sea ice model (LIM2; Fichefet and Morales Maqueda, 1997). The NEMO3.4 has a horizontal resolution of nominal 0.5º with 31 vertical levels in the rescaled z* height coordinate. In the OPA9, the vertical eddy

https://doi.org/10.5194/egusphere-2025-2258
Preprint. Discussion started: 28 May 2025

viscosity and diffusivity coefficients are computed from a turbulent kinetic energy (TKE) closure model after several modifications (Blanke and Delecluse, 1993; Madec et al., 1998). The lateral turbulence Is also associated to an eddy-induced velocity using a parameterization of mesoscale eddy-induced turbulence (Gent and McWilliams, 1990). The OPA9 was initialized with monthly climatology of ocean temperature and salinity in January from the Levitus dataset (Levitus, 1982) with no motion. The LIM2 includes the sea ice dynamics based on the viscous-plastic (VP; Hibler, 1979) rheology and the modified three-layer (two-layer sea ice and one-layer snow) thermodynamic formulation (Semtner, 1976). The atmospheric component of the SINTEX-F2 is based on the ^{5t}h version of the ECMWF and MPI-M in Hamburg (ECHAM5.4; Roeckner et al., 2003) atmospheric model. The ECHAM5.4 has a horizontal resolution of T106 (approximately 125 km at the Equator) with 31 vertical levels up to 1 hPa. It also adopted Nordeng (1994) parameterization for cumulous convection. The surface heat flux, momentum, and freshwater are exchanged between the atmosphere and ocean every two hours with no flux correction using the third version of the Ocean Atmosphere Sea Ice Soil (OASIS3; Valcke et al., 2004) coupler.

To compare with the eddy-parameterized coupled model, we developed the third version of the eddy-permitting SINTEX-F (SINTEX-F3) model. The oceanic component of the SINTEX-F3 is based on the NEMO4.0 (Madec, 2019) system which comprises the OPA ocean model and the SI^3 (Vancoppenolle et al., 2023) sea ice model. The major differences with the NEMO3.4 include the new sea ice model and the ocean model parameterization for the vertical mixing induced by the internal waves (St. Laurent et al., 2002) and surface waves (Qiao et al., 2010). The NEMO4.0 has a horizontal resolution of nominal 0.25° with 75 vertical levels in the rescaled z* height coordinate. The OPA uses the TKE turbulent closure model (Blanke and Delecluse, 1993; Madec, 1998) for the vertical eddy viscosity and diffusivity coefficients. For the lateral mixing, the OPA used a bilaplacian mixing which explicitly calculates the fourth order diffusion on tracers and momentum. The OPA was initialized with monthly climatology of ocean temperature and salinity in January from the World Ocean Atlas 2013 (WOA13; Locarnini et al., 2013, Zweng et al., 2013) dataset with no motion. The SI^3 includes the sea ice dynamics based on the elastic-viscous-plastic (EVP; Bouillon et al., 2013) rheology, multiple ice categories to represent subgrid-scale ice thickness (Thorndike et al., 1975), and multi-layer halo-thermodynamics including brine dynamics (Vancoppenolle et al., 2009). The atmospheric component of the SINTEX-F2 is based on the ECHAM6 (Giorgetta et al., 2013) atmospheric model. The ECHAM6 has a horizontal resolution of T255 (approximately 60 km at the Equator) with 95 vertical levels up to 0.01 hPa and adopted Nordeng (1994) parameterization

https://doi.org/10.5194/egusphere-2025-2258
Preprint. Discussion started: 28 May 2025

for cumulous convection. The major differences with the ECHAM5 invlove land processes based on the land vegetation JSBACH (Raddatz et al., 2007) model, the modified radiation schemes, the computation of surface albedo, and the triggering condition for convection. The surface heat flux, momentum, and freshwater are exchanged between the atmosphere and ocean every one hour with no flux correction by using the (OASIS-MCT; Valcke et al., 2013) coupler.

Both the SINTEX-F2 and SINTEX-F3 models were run over 100 years under the atmospheric radiative forcing set to be constant at the 1850 level in the pre-industrial era. We removed the first 32 years as a spin-up period, then analyzed the 42 years from the spin-up period for comparison with the observation and reanalysis product. Considering the model drift over the analysis period (e.g., 0.36 ºC and -0.47 ºC for the global mean surface air temperature of SINTEX-F2 and SINTEX-F3), we remove a linear trend from the variables. Details of the SINTEX-F2 and SINTEX-F3 configurations are summarized in Table 1.

2.3. CMIP6 HighResMIP models

For comparison with the SINTEX-F2 and SINTEX-F3 models, we adopted 13 available climate models participating in the High Resolution Model Intercomparison Project (HighResMIP; Haarsma et al., 2016) endorsed by CMIP6. The models include CESM1-CAM5-SE-LR and CESM1-CAM5-SE-HR (Hurrell et al., 2020; Chang et al., 2020), CMCC-CM2-HR4 and CMCC-CM2-VHR4 (Cherchi et al., 2019), ECMWF-IFS-LR, ECMWF-IFS-MR, and ECMWF-IFS-HR (Roberts et al., 2018), HadGEM3-GC31-LL, HadGEM3-GC31-MM, HadGEM3-GC31-HM and HadGEM3-GC31-HH (Roberts et al., 2019), and MPI-ESM1-2-HR and MPI-ESM1-2-XR (Gutjahr et al., 2019), respectively. Details of each model configuration and resolution are summarized in Table 2. Depending on the ocean model resolutions, we categorize 13 models into 3 low-resolution (CMIP6-LR) models with the ocean resolution of nominal 1º and 10 high-resolution (CMIP6-HR) models with the ocean resolutions of nominal 0.1º-0.4º. We analyzed the first 42 years of the 100 years control simulation under the 1950's constant radiative forcing (control-1950) after the 30-50 years spin-up period.

2.4. Climate indicators

To characterize global ocean and sea ice variability on an interannual timescale, we adopted the conventionally used climate indices based on the area-averaged SST and area-aggregated sea ice extent (SIE), respectively. In the tropics, we used the NINO3.4 index (170ºW-120ºW,

https://doi.org/10.5194/egusphere-2025-2258
Preprint. Discussion started: 28 May 2025

5ºS-5ºN) for ENSO, the Dipole Mode index (50ºE-70ºE, 10ºS-10ºN minus 90ºE-110ºE, 10ºS-Eq) for the IOD, and the ATL3 index (20ºW-Eq, 3ºS-3ºN) for the Atlantic Niño/Niña. In the western boundary current regions, we calculated the area-averaged SST index over the Agulhas Retroflection Current (15ºE-30ºE, 42ºS-40ºS), Brazil-Malvinas Current (55ºW-52ºW, 45ºS-36ºS), East Australian Current (150ºE-155ºE, 40ºS-30ºS), Gulf Stream (75ºW-40ºW, 35ºN-48ºN), and Kuroshio-Oyashio (142ºE-147ºE, 36ºN-41ºN) regions. In the eastern boundary current regions, we calculated the area-averaged SST index over the Dakar Niño/Niña (21ºW-17ºW, 9ºN-14ºN), Benguela Niño/Niña (8ºE-14ºE, 20ºS-10ºS), Ningaloo Niño/Niña (108ºE-115ºE, 28ºS-22ºS), California Niño/Niña (120ºW-130ºW, 20ºN-30ºN), and Chile Niño/Niña (80ºW-70ºW, 35ºS-20ºS). In the polar regions, we calculated the Antarctic and Arctic SIE, which is the total area of the SIC greater than 15%. For all indices, we calculate the detrended anomalies by subtracting the monthly climatology and linear trend using the least-squares method.

3. Results

3.1 Mean state bias

A brief understanding of model bias in the mean state allows us to better interpret the model bias in global ocean and sea ice variability on an interannual timescale. Figure 1 displays annual mean of the observed SST and climate model biases (i.e., model minus observation). Compared to the observed SST (Fig. 1a), the SINTEX-F2 (Fig. 1b) shows warm SST biases in the tropics, the western and eastern boundary current regions, and the Southern Ocean, whereas the model shows cold SST biases in the midlatitude open waters and the Arctic Sea. The warm biases remarkably reduce in the SINTEX-F3 (Fig. 1c), but cold biases prevail in the mid-high latitude oceans. On the other hand, the CMIP6-LR (Fig. 1d; average of 3 models) shows cold biases over global oceans except the Southern Ocean with a warm bias. The model biases decrease in the CMIP6-HR partly due to a greater number of models participating in the CMIP6-HR (Fig. 1e; average of 13 models), but the warm biases slightly appear in the tropical and subtropical oceans. Inspecting each climate model (Fig. S1), the spatial patterns of the warm and cold biases in the SINTEX-F3 (Fig. S1b) resemble those in the MPI-ESM1-2-XR (Fig. S1p). The MPI-ESM1-2-XR represents stronger cold bias than the lower-resolution MPI-ESM1-2-HR (Fig. S1o). Since both models employ the same atmospheric model but difference ocean and sea ice models, a source of the cold bias in the SINTEX-F3 could be attributed to the radiation

https://doi.org/10.5194/egusphere-2025-2258
Preprint. Discussion started: 28 May 2025

imbalance in the same atmospheric model (i.e., ECHAM6), as will be described later in Sect. 4.

The SST bias in the high latitudes is closely related to the sea ice bias in the climate models. In the Antarctic Sea, the observation data (Fig. 2a, b) shows that the SIE reaches its minimum in February and maximum in September. The SINTEX-F2 underestimates the observed SIE by about a half, mostly due to low SIC and warm SST biases in the Southern Ocean (Figs. 1b, 2c). In contrast, the SINTEX-F3 (Fig. 2b) reasonably captures the observed SIE, although the model overestimates austral winter SIE probably due to the high SIC bias in the Pacific and Atlantic sectors (Figs. 1c, 2d). The CMIP6-LR (Fig. 2b, e), on the other hand, represents larger SIE and SIC biases in the Antarctic Sea. The CMP6-HR (Fig. 2b, f) captures the observed SIE fairly well, although the model underestimates the SIC in the Indian sector that offsets the high SIC bias in the northern Weddell Sea and the Ross Sea. Among the CMIP6-HR models (Fig. S2), the spatial pattern of the SIC bias in the SINTEX-F3 (Fig. S2c) resembles that in the MPI-ESM1-2-HR (Fig. S2o).

In the Arctic Sea, the observation data (Fig. 3a, b) shows that the SIE reaches its minimum in September and maximum in March. The SINTEX-F2 (Fig. 3b, c) captures the observed SIE fairly well, although the model overestimates the SIC in the Greenland Sea and Barents Sea. The Arctic SIE is simulated to be larger in the SINTEX-F3 (Fig. 3b, d), mostly due to high SIC bias in the Bering Sea, Okhotsk Sea, and Baffin Bay as well as the Greenland Sea and Barents Sea. This is related to cold bias in those regions (Fig. 1c). The spatial pattern of the SIC bias in the CMIP6-LR (Fig. 3e) looks similar to the SINTEX-F3 (Fig. 3d), whereas the high SIC bias reduces remarkably in the CMIP6-HR (Fig. 3f), closer to the observed SIE. Among the CMIP6-HR models (Fig. S3), the spatial pattern of the SIC bias in the SINTEX-F3 (Fig. S3c) resembles that in the MPI-ESM1-2-XR (Fig. S3p). The difference in the SIC bias between the Antarctic and Arctic Seas suggests that a source of sea ice bias is related not only to the atmospheric model but to the ocean and sea ice models in the polar regions.

3.2. Tropical climate variability

Interannual climate variations in the tropics, which are described by the SST variability in some specific regions, affect global climate through atmospheric teleconnection. Figure 4 shows monthly standard deviation of the SST variability associated with three major climate phenomena in the tropics. The observed ENSO, which is measured by the NINO3.4 index, shows a strong seasonality with its peak in December (Fig. 4a). The SINTEX-F2 captures the

https://doi.org/10.5194/egusphere-2025-2258
Preprint. Discussion started: 28 May 2025

SST variability from April to July, but represents a weaker peak than the observation data. The SINTEX-F3 also captures the SST variability in June and July, but fails in simulating the peak in boreal winter. Both the CMIP6-LR and CMIP6-HR, on the other hand, reasonably simulate the observed SST variability with its peak in boreal winter, although both models show no distinct differences in the amplitude of the SST variability.

The IOD, which is determined with the Dipole Mode index, undergoes a strong seasonal variation with its peak in October (Fig. 4b). Both the SINTEX-F2 and SINTEX-F3 capture the observed SST variability very well, but tend to simulate the peak in August, two months earlier than the observation. Given the partial interaction between the IOD and ENSO, the weaker IOD signals simulated in the SINTEX-F2 and SINTEX-F3 may be attributed to the models' underestimation of ENSO strength (Fig. 4a). On the other hand, both the CMIP6-LR and CMIP6-HR simulate the peak of the SST variability in October and September, respectively, overestimating the amplitude of the observed SST variability.

The observed Atlantic Niño/Niña, which is evaluated with the ATL3 index, represents its peak in June (Fig. 4c). While the SINTEX-F2 fails to capture both the peak amplitude and the seasonal phase, the SINTEX-F3 shows some improvement, reproducing a modest peak in June. The CMIP6-LR, on the other hand, represents a stronger peak in July, whereas the CMIP6-HR captures the observed peak in June with a comparable magnitude. Both models show distinct differences in the amplitude of the SST variability, suggesting the importance of higher ocean resolutions for better representation of the Atlantic Niño/Niña. Since the Atlantic Niño/Niña also partly interacts with ENSO, the weaker Atlantic Niño/Niña signals in the SINTEX-F2 and SINTEX-F3 may also be related to the weaker ENSO signals simulated in the models (Fig. 4a).

To explore the impact of ENSO over global oceans, we calculated the regression of December-February SST anomalies onto the NINO3.4 index (Fig. 5). The observed SST shows warmer temperature in the central-eastern tropical Pacific and colder temperature in the western tropical Pacific, representing a canonical El Niño pattern. It is also associated with warmer temperature in the western Indian Ocean. Both the SINTEX-F2 and SINTEX-F3 (Fig. 5b, c) reproduce the observed SST pattern, but the simulated amplitude is much weaker in the SINTEX-F3, as expected from the weaker NINO3.4 index (Fig. 4a). Both the CMIP6-LR and CMIP6-HR (Fig. 5d, e), on the other hand, reasonably capture the observed SST pattern with comparable magnitudes. Among the CMIP6-HR models (Fig. S4), the MPI-ESM1-2-XR (Fig. 5p) shows the weakest SST pattern, resembling the SINTEX-F3 (Fig. S4c). These results

https://doi.org/10.5194/egusphere-2025-2258
Preprint. Discussion started: 28 May 2025

suggest that similar SST bias in both models (Fig. S1c, p) may have some links to simulation of weaker El Niño/La Niña, as will be detailed later in Sect. 4.

To evaluate the general atmospheric teleconnection associated with ENSO, we regressed December-February SLP anomalies onto the NINO3.4 index (Fig. 6). The reanalysis product (Fig. 6a) shows lower pressure in the central and eastern tropical Pacific and higher pressure in the western tropical Pacific, representing a weaker Walker Circulation associated with El Niño. In the mid-high latitudes, this is associated with a stronger Aleutian Low in the North Pacific and a weaker Amundsen Sea Low in the Southern Ocean. The SINTEX-F2 (Fig. 6b) captures the atmospheric teleconnection albeit a weaker amplitude, whereas the SINTEX-F3 (Fig. 6c) represents much weaker teleconnection to the extratropical region, which is mostly due to a weaker ENSO simulated in the model (Fig. 5c). Both the CMIP6-HR and CMIP6-LR (Fig. 6d, e), on the other hand, reasonably simulate the teleconnection pattern in the reanalysis product, as anticipated from the SST regression maps (Fig. 5d, e). Among the CMIP6-HR (Fig. S5), the MPI-ESM1-2-XR (Fig. 5p) simulates a weaker atmospheric teleconnection, similar to the SINTEX-F3. These results suggest that realistic simulation of the NINO3.4 index is required for better presentation of the atmospheric teleconnection associated with ENSO.

The SST teleconnection associated with the IOD (Fig. S6) also shows similar tendencies. The observation data (Fig. S6a) shows that a positive (negative) IOD, which is characterized by the colder temperature in the eastern tropical Indian Ocean and warmer temperature in the western tropical Indian Ocean, is associated with a canonical El Niño (La Niña) in the tropical Pacific. The association with El Niño is well reproduced in the SINTEX-F2 (Fig. S6b) and some of the CMIP6-LR and CMIP6-HR models. The SINTEX-F3 (Fig. S6c), on the other hand, simulates the IOD with no significant SST signals in the tropical Pacific. This is also seen in the other CMIP6-LR and CMIP6-HR models such as the ECMWF-IFS-LR (Fig. S6h), HadGEM3-GC31-HM (Fig. S6m), HadGEM3-GC31-HH (Fig. S6n), and MPI-ESM1-2-XR (Fig. S6p). These results suggest that some low- and medium-resolution ocean models like the SINTEX-F3 are capable of capturing inherent IOD dynamics that allow it to develop independently of El Niño/La Niña events.

For the Atlantic Niño/Niña, the observation data (Fig. S7a) represents that the Atlantic Niño (Niña), which is characterized by warmer (cooler) temperature in the central and eastern tropical Atlantic, is associated with a weak La Niña (El Niño) in the tropical Pacific. The SINTEX-F2 (Fig. S7b) simulates a weaker Atlantic Niño/Niña than the observation data, but there are no significant SST signals in the tropical Pacific. The SINTEX-F3 (Fig. S7c), on the other hand, simulates a weaker Atlantic Niño associated with a weak La Niña in the tropical

https://doi.org/10.5194/egusphere-2025-2258
Preprint. Discussion started: 28 May 2025

Pacific, closer to the observation data. Some of the CMIP6-LR and CMIP6-HR models (e.g., Fig. 7Sf, h, i, o) capture the association with a weak La Niña, while others simulate the Atlantic Niño independently. These results also suggest that the Atlantic Niño/Niña can occur in the absence of El Niño/La Niña in some of the low- and high-resolution ocean models.

3.3. Climate variability in the western boundary current regions

In the western boundary current region, ocean mesoscale eddies play prominent roles in generating the SST variability locally and affecting the overlying atmosphere. Figure 7 displays the monthly standard deviation of the SST anomalies averaged over the western boundary current regions. The Agulhas Retroflection Current and Brazil-Malvinas Current regions (Fig. 7a, b) exhibit a remarkable increase in the SST variability from the low- to high-resolution ocean models, closer to the observation. In the East Australian Current region (Fig. 7c), the CMIP6-HR shows a similar increase in the SST variability, while the SINTEX-F3 exhibits both increase and decrease relative to the SINTEX-F2, resulting in a closer agreement with the observation. In contrast, both SINTEX-F3 and CMIP6-HR overestimate the SST variability in the Gulf Stream and Kuroshio-Oyashio regions (Fig. 7d, e).

To describe how reasonably the ocean and atmospheric variability is simulated in the western boundary current regions, we calculated the regression of the January-March mean SST, net surface heat flux, and SLP anomalies onto the SST anomalies averaged over the Agulhas Retroflection Current region (see black boxes in Figs. 8-10) as an example of the western boundary current. Note that the box region corresponds to a region with the highest SST variability along the Agulhas Retroflection Current. The observation data (Fig. 8a) shows significantly warmer SST south of South Africa, and the SST signal is higher in the box region. The SINTEX-F2 (Fig. 8b) and CMIP6-LR (Fig. 8d) simulate a zonally-elongated structure of warmer SST, but these low-resolution ocean models cannot simulate the higher SST signal in the box region. The SINTEX-F3 (Fig. 8c), similar to the CMIP6-HR (Fig. 8e), captures the enhanced SST signal within the box region, although it fails to reproduce the zonally-elongated structure of the warmer SST. The limited higher SST are simulated by some of the CMIP6-HR models (Fig. S8). These results suggest that better representation of the higher SST variability in the Agulhas Retroflection Current region may be related to the increased ocean model resolutions.

We obtain similar results for the net surface heat flux regressions (Fig. 9). The reanalysis product (Fig. 9a) represents negative values in the Agulhas Retroflection Current

https://doi.org/10.5194/egusphere-2025-2258
Preprint. Discussion started: 28 May 2025

region, indicating that more heat comes out of the ocean driving the atmosphere. This is mostly due to the increase in the turbulent heat fluxes associated with the warmer SST. The negative values in the Agulhas Retroflection Current region are also found for both the low- and high-resolution ocean models (Fig. 9b-e), but the amplitude and spatial pattern in the SINTEX-F3 (Fig. 9c) and CMIP6-HR (Fig. 9e) resemble those in the reanalysis product. We also find the strong negative values in the Agulhas Retroflection Current region among the CMIP6-HR models (Fig. S9). These results indicate that realistic simulation of the higher SST variability in the Agulhas Retroflection Current region (Fig. 8c, e) leads to better representation of the air-sea interaction in the region.

The SLP regressions, on the other hand, do not show remarkable differences in the amplitude and spatial patterns (Fig. 10). The reanalysis product (Fig. 10a) represents higher SLP values south of the Agulhas Retroflection Current region. The higher SLP values south of the Agulhas Retroflection Current region are also found in the low- and high-resolution ocean models (Fig. 10b-e). Both models represent comparable magnitude and spatial pattern of the higher SLP values. We can also find the similar structure of the higher SLP values among the CMIP6-HR models (Fig. S10) except the CMCC-CM2-HR4 (Fig. S10f). These results indicate that the increased ocean resolution has a limited impact on the large-scale atmospheric variability in the Agulhas Retroflection Current region.

We also obtain similar results in the Brazil-Malvinas Current region where the SST variability improves with remarkable increase from the low- to high-resolution ocean models. The high-resolution ocean models (SINTEX-F3 and CMIP6-HR models; Fig. S11) tend to capture a fine structure of the SST variability with higher amplitude in the confluence zone of the Brazil-Malvinas Current than the low-resolution ocean models (SINTEX-F2 and CMIP6-LR models; Fig. S11). This leads to more negative surface heat flux values (Fig. S12) associated with the increased evaporation from the ocean surface in the confluence zone, although some of the CMIP6-HR models (MPI-ESM1-2-HR and MPI-ESM1-2-XR; Fig. S12o, p) show positive surface heat flux values. On the other hand, both low- and high-resolution models can simulate the strengthening of the anticyclonic circulation southeast of the confluence zone (Fig. S13). This contributes to the reduced evaporation associated with the southwestward advection of warm and wet air from the subtropics, counteracting the negative surface heat flux values in the confluence zone (Fig. S12). Therefore, the negative surface heat flux values in the confluence zone are caused by the warm SST values, and the increased ocean resolution is crucial for realistically simulating the air-sea interaction in the western boundary current regions.

https://doi.org/10.5194/egusphere-2025-2258
Preprint. Discussion started: 28 May 2025

3.4. Climate variability in the eastern boundary current regions

The eastern boundary current is not so strong as the western boundary current, but coastal air-sea interaction in the eastern boundary current involves the ocean mesoscale eddies and plays an important role in developing the coastal Niño/Niña. Figure 11 shows the monthly standard deviation of the SST variability in the coastal Niño/Niña region (see the definition in Sect. 2.4). The SST variability associated with the Dakar Niño/Niña increases during the peak season of February-April with the increased ocean model resolution, closer to the observation (Fig. 11a). We also find a moderate increase of the SST variability associated with the Benguela Niño/Niña during the peak season of March-May (Fig. 11b). The other three coastal Niño/Niña (Fig. 11c-e), on the other hand, do not represent much increase but neutral state or decrease in the SST variability with the increased ocean model resolution, except the California Niño/Niña in the SINTEX-F3 (Fig. 11d). Since these coastal Niño/Niña are more influenced by ENSO because of the proximity to the tropical Pacific, the influence of the ocean mesoscale eddies on the SST variability may be overwhelmed by the large-scale atmospheric and oceanic teleconnection associated with ENSO.

Figures 12-14 show the regressions of SST, net surface heat flux, and SLP anomalies onto the SST anomalies averaged over the Dakar Niño/Niña region (see black boxes in Figs. 12-14) as an example of the eastern boundary current region. The observation data (Fig. 12a) shows a basin-wide warmer SST in the North Atlantic which peaks off Dakar. Both the low- and high-resolution ocean models (Fig. 12b-e) capture the basin-wide warmer SST in the North Atlantic, but the SST variability off Dakar is simulated to be higher in the high-resolution ocean models (Fig. 12c, e). We also find the higher SST variability among most of the CMIP-HR (Fig. S14) except the CESM1-CAM5-SE-HR (Fig. S14e). The increased ocean resolution appears to help better simulate the coastal SST variability associated with the Dakar Niño/Niña.

We find similar tendencies for the net surface heat flux regressions (Fig. 13). The reanalysis product (Fig. 13a) shows negative values off Dakar. This corresponds well to the higher SST variability there (Fig. 12a). This is mostly due to increase in the turbulent heat flux, indicating the ocean driving the atmosphere. The low-resolution ocean models (Fig. 13b, d) cannot simulate the significantly negative surface heat flux values, but the high-resolution ocean models (Fig. 13c, e) capture the negative values off Dakar properly, although the SINTEX-F3 does not simulate significantly positive values in the subtropical open ocean. The negative values are also well captured among the CMIP6-HR models (Fig. S15) except the

https://doi.org/10.5194/egusphere-2025-2258
Preprint. Discussion started: 28 May 2025

CESM1-CAM5-SE-HR (Fig. S15e). These results indicate that better representation of the SST variability associated with Dakar Niño/Niña leads to that of the surface heat flux variability off Dakar.

Both the low- and high-resolution ocean models, however, represent no distinct difference in the atmospheric variability associated with the Dakar Niño/Niña. The reanalysis (Fig. 14a) shows negative SLP values in the North Atlantic. This leads to weakening of the trade winds and shoaling of the mixed layer thereby absorbing shortwave radiation more efficiently, responsible for development of the warmer SST there (Oettli et al., 2016). Both low- and high-resolution ocean models (Fig. 14b-e) well reproduce the negative SLP values with comparable magnitude and spatial pattern. Most of the CMIP6-HR models (Fig. S16) except the CMCC-CM2-HR4 (Fig. S16f), ECMWF-IFS-HR (Fig. 16j), and HadGEM3-GC31-HH (Fig. 16n) well capture the negative SLP values in the North Atlantic. These results indicate that the increased ocean model resolution has little impact on the large-scale atmospheric variability in the North Atlantic.

We also obtain similar results in the Benguela Niño/Niña region where the SST variability shows moderate improvement with the increased ocean model resolution. The high-resolution ocean models (SINTEX-F3 and CMIP6-HR; Fig. S17) tend to simulate higher SST variability near the west coast of Angola and Namibia than the low-resolution ocean models (SINTEX-F2 and CMIP6-LR; Fig. S17). This leads to negative surface heat flux values (Fig. S18) associated with the increased evaporation from the ocean surface, although some of the models (SINTEX-F3, MPI-ESM1-2-HR, MPI-ESM-1-2-XR; Fig. S18c, o, p) show the positive values. The SLP regressions (Fig. S19), on the other hand, show weakening of the subtropical high, the St. Helena High, in the South Atlantic, which brings warm and dry air from the tropics to suppress the evaporation, counteracting the negative surface heat flux values near the west coast of Angola and Namibia (Fig. S18). There are small differences in the SLP values between the high and low-resolution models, so the increased ocean model resolution is important for reproducing the air-sea interaction in the eastern boundary current regions.

3.5 Polar climate variability

In the polar regions, not only the increased ocean model resolution but also the improved sea ice model physics influence the representation of sea ice variability. Figure 15 shows the monthly standard deviation of the Antarctic and Arctic SIE anomalies. The observation data (Fig. 15a) shows that Antarctic SIE variability peaks in austral summer. Antarctic SIE

https://doi.org/10.5194/egusphere-2025-2258
Preprint. Discussion started: 28 May 2025

variability increases remarkably with the increased ocean model resolution, although the high-resolution ocean models overestimate the observed SIE variability (Fig. 15a). The Arctic SIE variability, on the other hand, reaches its peak in boreal fall (Fig. 15b). The Arctic SIE variability decreases remarkably from the CMIP6-LR to the CMIP6-HR, closer to the observation. The SINTEX-F3 shows higher SIE variability than the SINTEX-F2, overestimating the observation. These results indicate that the impact of the increased ocean model resolution and the improved sea ice model physics on the representation of the sea ice variability appears to differ between the Antarctic and the Arctic Sea.

To evaluate how reasonably the sea ice and atmospheric variability is simulated in the models, we regressed the SIC with net surface heat flux, and SLP anomalies onto the Antarctic SIE anomalies during austral summer (Figs. 16-18). Observations (Fig. 16a) indicate higher SIC in the Weddell Sea and Ross Sea. While the low-resolution ocean models (Fig. 16b, d) significantly underestimate the SIC in these regions, the high-resolution ocean models (Fig. 16c, e) better capture both the amplitude and spatial pattern of the observed high SIC. However, among the CMIP6-HR models (Fig. S20), there remains considerable diversity in the strength and spatial pattern of the simulated SIC.

We obtain similar results for the net surface heat flux (Fig. 17). The reanalysis product (Fig. 17a) shows negative values in the Weddell Sea and the Ross Sea, corresponding well to the higher SIC values (Fig. 16a). This indicates that more heat comes out of the ocean and sea ice to the atmosphere, contributing to the sea ice increase there. The low-resolution ocean models (Fig. 17b, d) simulate the negative values much weaker, but the high-resolution ocean models (Fig. 17c, e) can capture the amplitude and spatial pattern of negative values well. Among the CMIP6-HR models (Fig. S21), the models with higher SIC values tend to simulate the larger negative values of the net surface heat flux. These results indicate that better representation of the Antarctic sea ice variability is closely related to that of the surface heat flux variability in the Antarctic Sea.

The atmospheric circulation variability is also improved in the high-resolution ocean models. The reanalysis product (Fig. 18a) represents negative SLP values over Antarctica and positive values in the midlatitudes, exhibiting a positive phase of the Southern Annular Mode (SAM; Thompson and Wallace 2000). The positive SAM leads to strengthening of the westerlies thereby inducing the northward cold Ekman transport from the polar ocean on a seasonal timescale (Ferreira et al. 2015), contributing to the sea ice expansion. The SINTEX-F2 (Fig. 18b) fails in simulating the SLP variability, but the SINTEX-F3 (Fig. 18c) and CMIP6-LR (Fig. 18d) capture the spatial pattern well, although the statistical significance for the

CMIP6-LR is limited due to a smaller number of models. The high-resolution ocean models (Fig. 18c, e), on the other hand, reasonably capture the positive SAM structure in the mid-high latitudes, which is statistically significant. There is a large diversity in the spatial pattern and amplitude of the SLP values among the CMIP6-HR models (Fig. S22), but the models with a positive SAM (Fig. S22g, l, m) tend to simulate the higher SIC values in the Weddell Sea and Ross Sea.

In the Arctic region, on the other hand, the increased ocean resolution and the improved sea ice model have little impacts on simulation of the sea ice variability and the associated atmospheric variability. Figures S23-25 show regressions of the SIC, net surface heat flux, and SLP anomalies onto the Arctic SIE anomalies during boreal fall. The observation data (Fig. S23a) shows higher SIC values in the Kara Sea, Laptev Sea, East Siberian Sea, Chukchi Sea, and Beaufort Sea, but only the CESM1-CAM5-SE-LR (Fig. S23d), CESM1-CAM5-SE-HR (Fig. S23e), and MPI-ESM1-2-XR (Fig. S23p) models capture the spatial pattern of the higher SIC values in those regions. Other models tend to simulate higher SIC values in the Barents Sea and Greenland Sea. Both the reanalysis product and model simulations (Fig. S24) do not show robust signals of the surface heat flux in the Kara Sea, Laptev Sea, East Siberian Sea, Chukchi Sea, and Beaufort Sea, so the linkage between the surface heat flux variability and the sea ice variability is weak in those marginal seas. We also find the negative SLP values (Fig. S25) associated with the higher SIC values in the above marginal seas, but only the CESM1-CAM5-SE-LR (Fig. S25d) out of the above three successful models with realistic SIC values capture the negative SLP values there. These results suggest that the Arctic sea ice variability in those marginal seas may be driven by the ocean and sea ice processes rather than the atmospheric variability, which needs better representation of ocean and sea ice physics in the models.

4. Discussions

We have demonstrated some improvement in the mean state of SST and SIC from the low- to high-resolution ocean models, but among the high-resolution ocean models, the SINTEX-F3 represent the largest cold bias in the mid-high latitude oceans. To clarify a possible source of the cold SST bias, we describe the zonally-averaged ocean potential temperature, salinity, and potential density as a function of the depth over the analysis period (Figs. S26-28). Intriguingly, we find that the cold temperature bias in the SINTEX-F3 (Fig. S20c) is confined only in the upper 200-300 m, while the subsurface ocean shows a warm temperature

https://doi.org/10.5194/egusphere-2025-2258
Preprint. Discussion started: 28 May 2025

bias compared to the observation data (Fig. S26a). The vertical structure of temperature bias in the SINTEX-F3 resembles that in the MPI-ESM1-2-HR (Fig. S26o) and MPI-ESM1-2-XR (Fig. S26p), although there is some difference in the Antarctic Sea south of 60ºS.

The SINTEX-F3 (Fig. S27c) also shows fresher bias mostly in the upper 200-300 m of the midlatitude oceans and above the 1000 m of the polar oceans, whereas the model represents saltier bias in the deeper ocean compared to the observation (Fig. S27a). The fresher bias in the upper 1000 m of the polar region leads to lower density bias (Fig. S28c) compared to the observation (Fig. S28a), indicating the stronger stratification in the polar oceans. The stronger stratification prevents the mixed layer from entraining the warm subsurface water, contributing to the cold near-surface temperature bias in the polar oceans. The cold temperature bias in the upper 200-300 m between 60ºS and 60ºN (Fig. S26c), on the other hand, contributes to the higher density bias (Fig. S28c), indicating the weaker stratification in the tropics and midlatitudes. The weaker stratification enhances the mixed-layer deepening thereby entraining the subsurface cold water, contributing to the cold temperature bias in the tropics and midlatitudes.

Since the cold bias is confined in the upper ocean, the source of cold bias may originate from the atmospheric model. In this study, we analyzed the simulation results for all models after the 30-50 year spin-up period because of the constraint of computational resources for model simulations. Considering the ocean adjustment time, the spin-up periods are too short for the ocean models to drift from the initial ocean state. One may wonder if there exists the radiation imbalance at the top of the atmosphere in the climate models. To verify this possibility, we estimated the net downward radiation at the top of the atmosphere and the land/ocean surface, and their differences (Table 3). The SINTEX-F3 shows a comparable magnitude of the net downward radiation (0.56 W m^{-2}) at the top of the atmosphere against the ERA5 reanalysis product (0.50 W m^{-2}), which is about a half as small as the SINTEX-F2 (1.17 W m^{-2}) . The net surface heat flux in the SINTEX-F3 is considerably lower (1.14 W m^{-2}) than in the SINTEX-F2 (1.63 W m^{-2}), indicating less heat entering the ocean and land. Moreover, the difference between the top-of-the-atmosphere radiation and the net surface heat flux is more negative in the SINTEX-F3 (-0.58 W m^{-2}), about 26% larger in magnitude than in the SINTEX-F2 (-0.46 W m^{-2}). This increased heat loss in the SINTEX-F3 appears to contribute to the colder SST bias associated with a cooler atmospheric state compared to the SINTEX-F2.

The other possible reason for the cold bias in the SINTEX-F3 lies in differences in the radiative forcing used for running the control simulations. Both the SINTEX-F2 and SINTEX-F3 adopted the constant radiative forcing in the preindustrial period of 1850, whereas the

https://doi.org/10.5194/egusphere-2025-2258
Preprint. Discussion started: 28 May 2025

CMIP6 models used the forcing in 1950. For example, the CO2 concentration for the SINTEX-F3 is set to 285 ppm, which is lower by around 10 % than 311 ppm for the CMIP6 models. Also, we calculated the model bias against the observation data during the satellite period of 1982-2022, which is a warmer period than the preindustrial era.

Although the SINTEX-F3 represents a cold SST bias in the mean state, it better simulates interannual climate variability over the global oceans except the tropical Pacific than the SINTEX-F2. The cold SST bias may have limited impacts on the simulation of the interannual climate variability over the global oceans except the tropical Pacific, but the impact on ENSO cannot be ignored. For example, the SINTEX-F3 shows colder SST, shallower thermocline, and weaker trade winds (except July, August, and December) in the western tropical Pacific (Fig. S29a, c, e). The smaller warm water volume above the thermocline in the western tropical Pacific leads to weaker atmospheric convection and air-sea interaction thereby inducing weaker SST variability. In the eastern tropical Pacific, on the other hand, the SINTEX-F3 shows warmer SST (except May-July), shallower thermocline, and weaker trade winds than the observation/reanalysis product and the SINTEX-F2 (Fig. S29b, d, f). This leads to stronger ocean stratification that prevents vertical ocean processes from affecting the SST variability in the eastern tropical Pacific. These results suggest that a cold SST bias in the global oceans may contribute to a weaker Walker Cell and air-sea interaction in the tropical Pacific, responsible for the development of El Niño/La Niña. We need further efforts in improving the cold SST bias by reducing the radiation imbalance in the atmospheric model of the SINTEX-F3.

5. Conclusions

This study has demonstrated the pros and cons of the eddy-permitting models in simulating interannual climate variability over global oceans. Most of the eddy-permitting models show the limited improvement of simulation for the tropical climate variability such as ENSO (c.f., Liu et al., 2022), the IOD, and Atlantic Niño/Niña, indicating the limited benefits of the increased ocean model resolutions in the tropics. In the western and eastern boundary current regions, on the other hand, most of the models with the increased ocean model resolutions better capture the amplitude and spatial pattern of the SST variability and the associated surface heat flux variability (c.f., Bellucci et al., 2021), although the models show no distinct difference in the simulation of the associated large-scale atmospheric variability. The results suggest that accurately representing ocean mesoscale eddies is crucial for realistically simulating the SST and surface heat flux variability, particularly in the western and eastern boundary current regions. This is especially important for capturing the coastal Niño/Niña phenomena in certain eastern boundary areas. However, we should note the limited improvement of simulations in some of the extratropical regions. For example, the Kuroshio-Oyashio and Gulf Stream regions represent the limited improvement in simulation of the SST variability (An et al., 2023). These regions are more subject to westward-propagating ocean mesoscale eddies that originate from the central North Pacific and North Atlantic.

Furthermore, we find that models with higher ocean model resolutions more accurately reproduce the sea ice variability associated with atmospheric variability in the Antarctic Sea (see Selivanova et al., 2024a). This improvement is attributed not only to higher ocean model resolutions, but also to improved physics in the sea ice models. However, these higher-resolution ocean models do not significantly improve the simulation of Arctic sea ice variability (see Selivanova et al., 2024b). Arctic sea ice variability is more strongly influenced by the state of ocean and sea ice, suggesting the need for further refinement of both sea ice model physics and ocean model resolution, in addition to land surface processes in the regions. Further efforts in improving the model physics and resolutions for better representation of interannual climate variability are required and underway.

Code Availability

Sample codes to analyze and describe the model output will be available in an open website before publication.

Data Availability

The observed SST data is available from the NOAA's OISSTv2 website (https://psl.noaa.gov/data/gridded/data.noaa.oisst.v2.highres.html, Reynolds et al. 2007). The SIC data is also available from the NSIDC website (https://doi.org/10.5067/MPYG15WAA4WX, DiGirolamo et al., 2022). The subsurface ocean temperature and salinity data can also be obtained from the UK Met Office's EN4 website (https://www.metoffice.gov.uk/hadobs/en4/, Good et al. 2013). The atmospheric variables can be downloaded from the ECMWF and Copernicus Climate Data Store (https://doi.org/10.24381/cds.f17050d7, Hersbach et al., 2020). The HighResMIP model output can be downloaded from any of the CMIP6 ESGF nodes (https://esgf-ui.ceda.ac.uk/cog/search/cmip6-ceda/, Haarsma et al., 2016).

Author Contributions

Y. M., M. G., M. N., and S. B. designed this research. Y. M., E. M., S. M., C. R., and L. K., developed SINTEX-F3 model. Y. M. conducted and analyzed the SINTEX-F3 control simulation. All authors contribute to writing the manuscript.

Competing Interests

All authors do have no competing interests in this research.

Acknowledgments

We would like to acknowledge Earth Simulator for allowing us to run the control simulations of the SINTEX-F2 and SINTEX-F3 models for the purpose of this study. We would also like to thank the CMIP6 ESGF for providing us with the 1950-control simulations of the CMIP6 HighResMIP models. We are grateful to Drs. Yuya Baba, Takeshi Doi, Nobumasa Komori for providing helpful comments on the original work.

https://doi.org/10.5194/egusphere-2025-2258
Preprint. Discussion started: 28 May 2025

References

Aguedjou, H. M. A., Chaigneau, A., Dadou, I., Morel, Y., Baloïtcha, E., and Da-Allada, C. Y.: Imprint of mesoscale eddies on air-sea interaction in the tropical Atlantic Ocean, Remote Sensing, 15, 3087, https://doi.org/10.3390/rs15123087, 2023.

An, B., Yu, Y., Hewitt, H., Wu, P., Furtado, K., Liu, H., Lin, P., Luan, Y., and Chen, K.: The benefits of high-resolution models in simulating the Kuroshio Extension and its long-term changes, Clim. Dyn, 61, 5407-5427, https://doi.org/10.1007/s00382-023-06862-z, 2023.

An, S. I.: Interannual variations of the tropical ocean instability wave and ENSO, J. Climate, 21, 3680-3686, https://doi.org/10.1175/2008JCLI1701.1, 2008.

Auer, S. J.: Five-year climatological survey of the Gulf Stream system and its associated rings, J. Geophys. Res. Oce., 92, 11709-11726, https://doi.org/10.1029/JC092iC11p11709, 1987.

Bellucci, A., Athanasiadis, P. J., Scoccimarro, E., Ruggieri, P., Gualdi, S., Fedele, G., Haarsma, R. J., Garcia-Serrano, J., Castrillo, M., Putrahasan, D., Sanchez-Gomez, E., Moine, M. -P., Roberts, C. D., Roberts, M. J., Seddon, J., and Vidale, P. L.: Air-Sea interaction over the Gulf Stream in an ensemble of HighResMIP present climate simulations, Clim. Dyn., 56, 2093-2111, https://doi.org/10.1007/s00382-020-05573-z, 2021.

Blanke, B., and Delecluse, P.: Variability of the tropical Atlantic Ocean simulated by a general circulation model with two different mixed-layer physics, J. Phys. Oceanogr., 23, 1363-1388, https://doi.org/10.1175/1520-0485(1993)023<1363:VOTTAO>2.0.CO;2, 1993.

Bouillon, S., Fichefet, T., Legat, V., and Madec, G.: The elastic–viscous–plastic method revisited. Ocean Modelling, 71, 2-12, https://doi.org/10.1175/1520-0485(1993)023<1363:VOTTAO>2.0.CO;2, 2013.

Bowen, M. M., Wilkin, J. L., and Emery, W. J.: Variability and forcing of the East Australian Current, J. Geophys. Res. Oce., 110, https://doi.org/10.1029/2004JC002533, 2005.

Capet, X., Colas, F., Mcwilliams, J. C., Penven, P., and Marchesiello, P.: Eddies in eastern boundary subtropical upwelling systems, Ocean Modeling in an Eddying Regime, 177, 131-147, https://doi.org/10.1029/177GM10, 2008.

Chaigneau, A., Eldin, G., and Dewitte, B.: Eddy activity in the four major upwelling systems from satellite altimetry (1992–2007), Prog. Oceanogr., 83, 117-123, https://doi.org/10.1016/j.pocean.2009.07.012, 2009.

Chang, P., Zhang, S., Danabasoglu, G., Yeager, S. G., Fu, H., Wang, H., et al.: An unprecedented set of high-resolution earth system simulations for understanding multiscale interactions in climate variability and change, J. Adv. Model. Earth Syst., 12, e2020MS002298, https://doi.org/10.1029/2020MS002298, 2020.

Chelton, D. B., Schlax, M. G., Freilich, M. H., and Milliff, R. F.: Satellite measurements reveal persistent small-scale features in ocean winds, Science, 303, 978-983, https://doi.org/10.1126/science.1091901, 2004.

Chelton, D. B., Schlax, M. G., and Samelson, R. M.: Global observations of nonlinear mesoscale eddies, Prog. Oceanogr., 91, 167-216, https://doi.org/10.1016/j.pocean.2011.01.002, 2011.

Cheon, W. G., and Gordon, A. L.: Open-ocean polynyas and deep convection in the Southern Ocean, Sci. Rep., 9, 6935, https://doi.org/10.1038/s41598-019-43466-2, 2019.

Cherchi, A., Fogli, P. G., Lovato, T., Peano, D., Iovino, D., Gualdi, S., Masina, S., Scoccimarro, E., Materia, S., Bellucci, A., and Navarra, A.: Global mean climate and main patterns of variability in the CMCC-CM2 coupled model, J. Adv. Model. Earth Syst., 11, 185-209, https://doi.org/10.1029/2018MS001369, 2019.

DiGirolamo, N., Parkinson, C. L., Cavalieri, D. J., Gloersen, P. and Zwally, H. J.: Sea Ice Concentrations from Nimbus-7 SMMR and DMSP SSM/I-SSMIS Passive Microwave Data. (NSIDC-0051, Version 2), NASA National Snow and Ice Data Center Distributed Active Archive Center, Boulder, Colorado USA, https://doi.org/10.5067/MPYG15WAA4WX, Date Accessed 03-28-2025, 2022.

Dong, D., Brandt, P., Chang, P., Schütte, F., Yang, X., Yan, J., and Zeng, J.: Mesoscale eddies in the northwestern Pacific Ocean: Three-dimensional eddy structures and heat/salt transports, J. Geophys. Res. Oce., 122, 9795-9813, https://doi.org/10.1002/2017JC013303, 2017.

Dufour, C. O., Morrison, A. K., Griffies, S. M., Frenger, I., Zanowski, H., and Winton, M.: Preconditioning of the Weddell Sea polynya by the ocean mesoscale and dense water overflows, J. Climate, 30, 7719-7737, https://doi.org/10.1175/JCLI-D-16-0586.1, 2017.

Feng, M., McPhaden, M. J., Xie, S. P., and Hafner, J.: La Niña forces unprecedented Leeuwin Current warming in 2011, Sci. Rep., 3, 1277, https://doi.org/10.1038/srep01277, 2013.

Fichefet, T., and Maqueda, M. M.: Sensitivity of a global sea ice model to the treatment of ice thermodynamics and dynamics, J. Geophys. Res. Oce., 102, 12609-12646, https://doi.org/10.1029/97JC00480, 1997.

Gent, P. R., and Mcwilliams, J. C.: Isopycnal mixing in ocean circulation models, J. Phys. Oceanogr., 20, 150-155, https://doi.org/10.1175/1520-0485(1990)020<0150:IMIOCM>2.0.CO;2, 1990.

Giorgetta, M. A., Roeckner, E., Mauritsen, T., Bader, J., Crueger, T., Esch, M., Rst, S., Kornblueh, L., Schmidt, H., Kinne, S., Hohenegger, C., Möbis, B., Krismer, T., Wieners, K. -H., and Stevens, B.: The atmospheric general circulation model ECHAM6-model description, Berichte zur Erdsystemforschung / Max-Planck-Institut für Meteorologie, 135, 177 pp., 2013.

Good, S. A., Martin, M. J., and Rayner, N. A.: EN4: Quality controlled ocean temperature and salinity profiles and monthly objective analyses with uncertainty estimates, J. Geophys. Res. Oce., 118, 6704-6716, https://doi.org/10.1002/2013JC009067, 2013.

Gouretski, V., and Cheng, L.: Correction for systematic errors in the global dataset of temperature profiles from mechanical bathythermographs, J. Atmos. Ocean. Technol., 37, 841-855, https://doi.org/10.1175/JTECH-D-19-0205.1, 2020.

Gouretski, V., and Reseghetti, F.: On depth and temperature biases in bathythermograph data: Development of a new correction scheme based on analysis of a global ocean database, Deep-Sea Res. I: Oceanogr. Res. Pap., 57, 812-833, https://doi.org/10.1016/j.dsr.2010.03.011, 2010.

Griffies, S. M., Winton, M., Anderson, W. G., Benson, R., Delworth, T. L., Dufour, C. O., Dunne, J. P., Goddard, P., Morrison, A. K., Rosati, A., Wittenberg, A. T., and Zhang, R.: Impacts on ocean heat from transient mesoscale eddies in a hierarchy of climate models, J. Climate, 28, 952-977, https://doi.org/10.1175/JCLI-D-14-00353.1, 2015.

Gruber, N., Lachkar, Z., Frenzel, H., Marchesiello, P., Münnich, M., McWilliams, J. C., Nagai, T., and Plattner, G. K.: Eddy-induced reduction of biological production in eastern boundary upwelling systems, Nat. Geo., 4, 787-792, https://doi.org/10.1038/ngeo1273, 2011.

Gutjahr, O., Putrasahan, D., Lohmann, K., Jungclaus, J. H., von Storch, J. S., Brüggemann, N., Haak, H., and Stössel, A.: Max planck institute earth system model (MPI-ESM1. 2) for the high-resolution model intercomparison project (HighResMIP). Geosci. Model Dev., 12, 3241-3281, https://doi.org/10.5194/gmd-12-3241-2019, 2019.

Haarsma, R. J., Roberts, M. J., Vidale, P. L., Senior, C. A., Bellucci, A., Bao, Q., Chang, P., Corti, S., Fučkar, N. S., Guemas, V., von Hardenberg, J., Hazeleger, W., Kodama, C., Koenigk, T., Leung, L. R., Lu, J., Luo, J.-J., Mao, J., Mizielinski, M. S., Mizuta, R., Nobre, P., Satoh, M., Scoccimarro, E., Semmler, T., Small, J., and von Storch, J.-S.: High Resolution Model Intercomparison Project (HighResMIP v1.0) for CMIP6, Geosci. Model Dev., 9, 4185–4208, https://doi.org/10.5194/gmd-9-4185-2016, 2016.

Hallberg, R.: Using a resolution function to regulate parameterizations of oceanic mesoscale eddy effects, *Oce. Model.*, *72*, 92-103, https://doi.org/10.1016/j.ocemod.2013.08.007, 2013.

Hersbach, H., Bell, B., Berrisford, et al.: The ERA5 global reanalysis, Q. J. R. Meteorol. Soc., 146, 1999-2049, https://doi.org/10.1002/qj.3803, 2020.

Hibler, W. D. III: A dynamic thermodynamic sea ice model, J. Phys. Oceanogr., 9: 815–846, https://doi.org/10.1175/1520-0485(1979)009<0815:ADTSIM>2.0.CO;2, 1979.

https://doi.org/10.5194/egusphere-2025-2258
Preprint. Discussion started: 28 May 2025

Hurrel, J., Holland, M., Gent, P., et al.: CMIP6 HighResMIP NCAR CESM1-CAM5-SE-LR control-1950, Earth System Grid Federation. https://doi.org/10.22033/ESGF/CMIP6.14271, 2020.

Itoh, S., and Yasuda, I.: Characteristics of mesoscale eddies in the Kuroshio–Oyashio Extension region detected from the distribution of the sea surface height anomaly, J. Phys. Oceanogr., 40, 1018-1034, https://doi.org/10.1175/2009JPO4265.1, 2010.

Kataoka, T., Tozuka, T., Behera, S., and Yamagata, T.: On the Ningaloo Niño/Niña, Clim. Dyn., 43, 1463-1482, https://doi.org/10.1007/s00382-013-1961-z, 2014.

Levitus, S.: Climatological atlas of the world ocean (Vol. 13), US Department of Commerce, National Oceanic and Atmospheric Administration, NOAA/ERL GFDL Professional Paper 13, Princeton, N.J., 173 pp. (NTIS PB83-184093), 1982.

Leyba, I. M., Saraceno, M., and Solman, S. A.: Air-sea heat fluxes associated to mesoscale eddies in the Southwestern Atlantic Ocean and their dependence on different regional conditions, Clim. Dyn., 49, 2491-2501, https://doi.org/10.1007/s00382-016-3460-5, 2017.

Li, X., Wang, Q., Danilov, S., Koldunov, N., Liu, C., Müller, V., Sidorenko, D., and Jung, T.: Eddy activity in the Arctic Ocean projected to surge in a warming world, Nat. Clim. Change, 14, 156-162, https://doi.org/10.1038/s41558-023-01908-w, 2024.

Liu, B., Gan, B., Cai, W., Wu, L., Geng, T., Wang, H., Jing, Z., and Jia, F.: Will increasing climate model resolution be beneficial for ENSO simulation?, Geophys. Res. Lett., 49, e2021GL096932, https://doi.org/10.1029/2021GL096932, 2022.

Locarnini, R. A., Mishonov, A.V., Antonov, J. I., Boyer, T. P., Garcia, H. E., Baranova, O. K., Zweng, M. M., Paver, C. R., Reagan, J. R., Johnson, D. R., Hamilton, M., and Seidov, D.: World Ocean Atlas 2013, Volume 1: Temperature. S. Levitus, Ed., A. Mishonov Technical Ed.; NOAA Atlas NESDIS 73, 40 pp, 2013.

https://doi.org/10.5194/egusphere-2025-2258
Preprint. Discussion started: 28 May 2025

Lutjeharms, J. R. E., and Valentine, H. R.: Eddies at the subtropical convergence south of Africa, J. Phys. Oceanogr., 18, 761-774, https://doi.org/10.1175/1520-0485(1988)018<0761:EATSCS>2.0.CO;2, 1988.

Madec, G.: NEMO ocean engine, Note du Pole de modélisation, Institut Pierre-Simon Laplace (IPSL), France. No 27. ISSN No 1288-1619, 2008.

Madec, G., Bourdallé-Badie, R., Chanut, J., et al.: NEMO ocean engine, Scientific Notes of Climate Modelling Center, 27 — ISSN 1288-1619, Institut Pierre-Simon Laplace (IPSL), https://doi.org/10.5281/zenodo.1464816, 2019.

Madec, G., Delecluse, P., Imbard, M., and Levy, C.: Opa 8 ocean general circulation model - reference manual, Tech. Rep., LODYC/IPSL Note 11, 1998.

Manley, T. O., and Hunkins, K.: Mesoscale eddies of the Arctic Ocean, *J. Geophys. Res. Oce.*, 90, 4911-4930, https://doi.org/10.1029/JC090iC03p04911, 1985.

Manucharyan, G. E., Thompson, A. F. Heavy footprints of upper-ocean eddies on weakened Arctic sea ice in marginal ice zones, Nat. Commun., 13, 2147, https://doi.org/10.1038/s41467-022-29663-0, 2022.

Masson, S., Terray, P., Madec, G., Luo, J. J., Yamagata, T., and Takahashi, K.: Impact of intra-daily SST variability on ENSO characteristics in a coupled model, Clim. Dyn., 39, 681-707, https://doi.org/10.1007/s00382-011-1247-2, 2012.

Melnichenko, O., Amores, A., Maximenko, N., Hacker, P., and Potemra, J.: Signature of mesoscale eddies in satellite sea surface salinity data, J. Geophys. Res. Oce., 122, 1416-1424, https://doi.org/10.1002/2016JC012420, 2017.

Meneghello, G., Marshall, J., Lique, C., Isachsen, P. E., Doddridge, E., Campin, J. M., Regan, H., and Talandier, C.: Genesis and decay of mesoscale baroclinic eddies in the seasonally ice-covered interior Arctic Ocean, J. Phys. Oceanogr., 51, 115-129, https://doi.org/10.1175/JPO-D-20-0054.1, 2021.

https://doi.org/10.5194/egusphere-2025-2258
Preprint. Discussion started: 28 May 2025

Messager, C., and Swart, S.: Significant atmospheric boundary layer change observed above an Agulhas Current warm cored eddy, Adv. Meteorol., 2016, 3659657, https://doi.org/10.1155/2016/3659657, 2016.

Morrison, A. K., Griffies, S. M., Winton, M., Anderson, W. G., and Sarmiento, J. L.: Mechanisms of Southern Ocean heat uptake and transport in a global eddying climate model, J. Climate, 29, 2059-2075, https://doi.org/10.1175/JCLI-D-15-0579.1, 2016.

Munday, D. R., Johnson, H. L., and Marshall, D. P.: Impacts and effects of mesoscale ocean eddies on ocean carbon storage and atmospheric pCO2. Global Biogeochem, Cycles, 28, 877-896, https://doi.org/10.1002/2014GB004836, 2014.

Nilsson, C. S., and Cresswell, G. R.: The formation and evolution of East Australian Current warm-core eddies. *Prog. Oceanogr.*, 9, 133-183, https://doi.org/10.1016/0079-6611(80)90008-7, 1980.

Nordeng, T. E.: Extended versions of the convective parametrization scheme at ECMWF and their impact on the mean and transient activity of the model in the tropics, Research Department Technical Memorandum, 206, 1-41, https://doi.org/10.21957/e34xwhysw, 1994.

Oettli, P., Morioka, Y., and Yamagata, T.: A regional climate mode discovered in the North Atlantic: Dakar Niño/Niña, Sci. Rep., 6, 18782, https://doi.org/10.1038/srep18782, 2016.

Ogata, T., and Masumoto, Y.: Interactions between mesoscale eddy variability and Indian Ocean dipole events in the Southeastern tropical Indian Ocean—case studies for 1994 and 1997/1998, Oce. Dyn., 60, 717-730, https://doi.org/10.1007/s10236-010-0304-4, 2010.

Pezzi, L. P., de Souza, R. B., Santini, M. F., et al.: Oceanic eddy-induced modifications to air–sea heat and CO2 fluxes in the Brazil-Malvinas Confluence, Sci. Rep., 11, 10648, https://doi.org/10.1038/s41598-021-89985-9, 2021.

Qiao, F., Yuan, Y., Ezer, T., Xia, C., Yang, Y., Lü, X., and Song, Z.: A three-dimensional surface wave–ocean circulation coupled model and its initial testing, Oce. Dyn., 60, 1339-1355, https://doi.org/10.1007/s10236-010-0326-y, 2010.

https://doi.org/10.5194/egusphere-2025-2258
Preprint. Discussion started: 28 May 2025

Qiu, B., and Chen, S.: Variability of the Kuroshio Extension jet, recirculation gyre, and mesoscale eddies on decadal time scales, J. Phys. Oceanogr., 35, 2090-2103, https://doi.org/10.1175/JPO2807.1, 2005.

Raddatz, T. J., Reick, C. H., Knorr, W., Kattge, J., Roeckner, E., Schnur, R., Wetzel, P., and Jungclaus, J.: Will the tropical land biosphere dominate the climate–carbon cycle feedback during the twenty-first century?, Clim. Dyn., *29*, 565-574, https://doi.org/10.1007/s00382-007-0247-8, 2007.

Reynolds, R. W., Smith, T. M., Liu, C., Chelton, D. B., Casey, K. S., and Schlax, M. G.: Daily high-resolution-blended analyses for sea surface temperature, J. Climate, 20, 5473-5496, https://doi.org/10.1175/2007JCLI1824.1, 2007.

Roberts, C. D., Senan, R., Molteni, F., Boussetta, S., Mayer, M., and Keeley, S. P. E.: Climate model configurations of the ECMWF Integrated Forecasting System (ECMWF-IFS cycle 43r1) for HighResMIP, Geosci. Model Dev., 11, 3681–3712, https://doi.org/10.5194/gmd-11-3681-2018, 2018.

Roberts, M. J., Baker, A., Blockley, E. W., Calvert, D., Coward, A., Hewitt, H. T., Jackson, L. C., Kuhlbrodt, T., Mathiot, P., Roberts, C. D., Schiemann, R., Seddon, J., Vannière, B., and Vidale, P. L.: Description of the resolution hierarchy of the global coupled HadGEM3-GC3.1 model as used in CMIP6 HighResMIP experiments, Geosci. Model Dev., 12, 4999–5028, https://doi.org/10.5194/gmd-12-4999-2019, 2019.

Roeckner, E., Bäuml, G., Bonaventura, et al.: The atmospheric general circulation model ECHAM 5. PART I: Model description, Max Planck Institute for Meteorology, 349, ISSN 0937-1060, 2003.

Rouault, M., Verley, P., and Backeberg, B.: Wind changes above warm Agulhas Current eddies, Ocean Sci., 12, 495–506, https://doi.org/10.5194/os-12-495-2016, 2016.

Saraceno, M., and Provost, C.: On eddy polarity distribution in the southwestern Atlantic, Deep-Sea Res. I: Oceanogr. Res. Pap., 69, 62-69, https://doi.org/10.1016/j.dsr.2012.07.005, 2012.

Sasaki, W., Richards, K. J., and Luo, J. J.: Impact of vertical mixing induced by small vertical scale structures above and within the equatorial thermocline on the tropical Pacific in a CGCM, Clim. Dyn., 41, 443-453, https://doi.org/10.1007/s00382-012-1593-8, 2013.

Selivanova, J., Iovino, D., and Cocetta, F.: Past and future of the Arctic sea ice in High-Resolution Model Intercomparison Project (HighResMIP) climate models, The Cryosphere, 18, 2739–2763, https://doi.org/10.5194/tc-18-2739-2024, 2024b.

Selivanova, J., Iovino, D., and Vichi, M.: Limited benefits of increased spatial resolution for sea ice in HighResMIP simulations, Geophys. Res. Lett., 51, e2023GL107969, https://doi.org/10.1029/2023GL107969, 2024a.

Semtner Jr, A. J.: A model for the thermodynamic growth of sea ice in numerical investigations of climate, J. Phys. Oceanogr., 6, 379-389, https://doi.org/10.1175/1520-0485(1976)006<0379:AMFTTG>2.0.CO;2, 1976.

Shannon, L. V., Boyd, A. J., Brundrit, G. B., and Taunton-Clark, J.: On the existence of an EI Niño-type phenomenon in the Benguela System, J. Mar. Res., 44. 495-520, 1986.

St. Laurent, L. C., Simmons, H. L., and Jayne, S. R.: Estimating tidally driven mixing in the deep ocean, Geophys. Res. Lett., 29, 21-1, https://doi.org/10.1029/2002GL015633, 2002.

Thompson, D. W., and Wallace, J. M.: Annular modes in the extratropical circulation. Part I: Month-to-month variability, J. Climate, 13, 1000-1016, https://doi.org/10.1175/1520-0442(2000)013<1000:AMITEC>2.0.CO;2, 2000.

Thorndike, A. S., Rothrock, D. A., Maykut, G. A., and Colony, R.: The thickness distribution of sea ice, J. Geophys. Res., 80, 4501–4513, https://doi.org/10.1029/JC080i033p04501, 1975.

Valcke, S.: The OASIS3 coupler: a European climate modelling community software, Geosci. Model Dev., 6, 373–388, https://doi.org/10.5194/gmd-6-373-2013, 2013.

Vancoppenolle, M., Fichefet, T., and Goosse, H.: Simulating the mass balance and salinity of Arctic and Antarctic sea ice. 2. Importance of sea ice salinity variations, Oce. Model., 27, 54-69, https://doi.org/10.1016/j.ocemod.2008.11.003, 2009.

Vancoppenolle, M., Rousset, C., Blockley, E., and the NEMO Sea Ice Working Group: SI3 – Sea Ice modelling Integrated Initiative – The NEMO Sea Ice Engine, Zenodo, https://doi.org/10.5281/zenodo.7534900, 2023.

Weijer, W., Veneziani, M., Stössel, A., Hecht, M. W., Jeffery, N., Jonko, A., Hodos, T., and Wang, H.: Local atmospheric response to an open-ocean polynya in a high-resolution climate model, J. Climate, 30, 1629-1641, https://doi.org/10.1175/JCLI-D-16-0120.1, 2017.

Willett, C. S., Leben, R. R., and Lavín, M. F.: Eddies and tropical instability waves in the eastern tropical Pacific: A review, Prog. Oceanogr., 69, 218-238, https://doi.org/10.1016/j.pocean.2006.03.010, 2006.

Williams, N. C., Scaife, A. A., and Screen, J. A.: Effect of increased ocean resolution on model errors in El Niño–Southern Oscillation and its teleconnections, Q. J. R. Meteorol. Soc., 150, 1489-1500, https://doi.org/10.1002/qj.4655, 2024.

Xue, J., Luo, J. J., Yuan, C., and Yamagata, T.: Discovery of Chile Niño/Niña, Geophys. Res. Lett., 47, e2019GL086468, https://doi.org/10.1029/2019GL086468, 2020.

Yu, J. Y., and Liu, W. T.: A linear relationship between ENSO intensity and tropical instability wave activity in the eastern Pacific Ocean, Geophys. Res. Lett., *30*, https://doi.org/10.1029/2003GL017176, 2003.

Yuan, C., and Yamagata, T.: California Niño/Niña, Sci. Rep., 4, 4801, https://doi.org/10.1038/srep04801, 2014.

https://doi.org/10.5194/egusphere-2025-2258
Preprint. Discussion started: 28 May 2025

Zhang, Z., Wang, W., and Qiu, B.: Oceanic mass transport by mesoscale eddies, Science, 345, 322-324, https://doi.org/10.1126/science.12524, 2014.

Zhang, Z., Zhang, Y., Wang, W., and Huang, R. X.: Universal structure of mesoscale eddies in the ocean, Geophys. Res. Lett., 40, 3677-3681, https://doi.org/10.1002/grl.50736, 2013.

Zweng, M. M, Reagan, J. R., Antonov, J. I., Locarnini, R. A., Mishonov, A. V., Boyer, T. P. Garcia, H. E., Baranova, O. K., Johnson, D. R., Seidov, D., Biddle, M. M.: World Ocean Atlas 2013, Volume 2: Salinity, S. Levitus, Ed., A. Mishonov Technical Ed.; NOAA Atlas NESDIS 74, 39 pp, 2013.

https://doi.org/10.5194/egusphere-2025-2258
Preprint. Discussion started: 28 May 2025

Tables

	SINTEX-F2	SINTEX-F3
Atmosphere-Land	ECHAM5.4 T106 (approx. 125 km) 31 levels (top 1 hPa) Cumulous convection: Nordeng (1994)	ECHAM6-JSBACH T255 (approx. 60 km) 95 levels (0.01 hPa) Cumulous convection: Nordeng (1994)
Ocean-Sea Ice	NEMO3.4-LIM2 Vertical mixing and diffusion: TKE closure model Lateral mixing: Gent and McWilliams (1990)	NEMO4.0-SI^3 Vertical mixing and diffusion: TKE closure model Lateral mixing: Bilaplacian mixing
Coupler	OASIS3	OASIS3-MCT
Radiative forcing	Pre-industrial level in 1850	Pre-industrial level in 1850
Time step	Atmosphere: 360 sec Ocean: 2400 sec Coupler: 7200 sec	Atmosphere: 90 sec Ocean: 900 sec Coupler: 3600 sec
Control simulation	100 years	100 years
CPU cores	128 cores (AMD EPYC 7742)	2238 cores (Same)
CPU times	2 hour per 1 year simulation	24 hour per 1 year simulation
Output size	12 GB per 1 year simulation (daily and monthly output)	360 GB per 1 year simulation (daily and monthly output)

Table 1 Configurations for the SINTEX-F2 and SINTEX-3 coupled models.

https://doi.org/10.5194/egusphere-2025-2258
Preprint. Discussion started: 28 May 2025

Model	**Atm+Lnd**	**Ocn+Sea Ice**	**Atm Res (km)**	**Ocn Res (deg)**	**Class**
CESM1-CAM5-SE-LR*	CAM5.2	POP2	100	1°	LR
CESM1-CAM5-SE-HR			25	0.25°	HR
CMCC-CM2-HR4	CAM4	NEMO3.6+CICE4	100	0.25°	HR
CMCC-CM2-VHR4			25	0.25°	HR
ECMWF-IFS-LR*	IFS cycle 43r1	NEMO3.4+LIM2	50	1°	LR
ECMWF-IFS-MR			50	0.25°	HR
ECMWF-IFS-HR			25	0.25°	HR
HadGEM3-GC31-LL*	GA/GL7.1	NEMO3.6+CICE5.1	250	1°	LR
HadGEM3-GC31-MM			100	0.25°	HR
HadGEM3-GC31-HM			50	0.25°	HR
HadGEM3-GC31-HH			50	0.1°	LR
MPI-ESM1-2-HR	ECHAM6.3	MPIOM1.6.3	100	0.4°	HR
MPI-ESM1-2-XR			50	0.4°	HR

Table 2 List of CMIP6 HighResMIP models used in this study. The models with asterisks correspond to the low-resolution (CMIP6-LR) models with the ocean resolution of 1°, whereas the models without asterisks are categorized into the high-resolution (CMIP6-HR) models with the ocean resolutions of 0.1-0.4°. Note that we categorize the models into the LR and HR models based on the ocean model resolutions.

https://doi.org/10.5194/egusphere-2025-2258
Preprint. Discussion started: 28 May 2025

Model	Qtoa	Qsfc	Qtoa-Qsfc
ERA5	0.50	5.79	-5.29
SINTEX-F2	1.17	1.63	-0.46
SINTEX-F3	0.56	1.14	-0.58
CESM1-CAM5-SE-LR*	N/A	1.41	N/A
CESM1-CAM5-SE-HR	N/A	1.20	N/A
CMCC-CM2-HR4	1.87	0.70	1.17
CMCC-CM2-VHR4	2.15	0.54	1.61
ECMWF-IFS-LR*	-0.60	1.47	-2.07
ECMWF-IFS-MR	-0.89	1.15	-2.04
ECMWF-IFS-HR	-0.74	1.03	-1.77
HadGEM3-GC31-LL*	0.21	1.13	-0.92
HadGEM3-GC31-MM	-0.00	0.85	-0.85
HadGEM3-GC31-HM	0.01	0.83	-0.82
HadGEM3-GC31-HH	0.05	0.88	-0.83
MPI-ESM1-2-HR	0.45	0.97	-0.52
MPI-ESM1-2-XR	0.30	0.90	-0.60

Table 3 Annual mean of globally averaged net top-of-the-atmosphere radiation (Qtoa; in W m^{-2}) and net surface heat flux (Qsfc; in W m^{-2}) for the ERA5 reanalysis (1982-2023) and climate models (42 years after the spin up period). Positive values indicate the heat going down from the top. The models with asterisks correspond to the low-resolution (CMIP6-LR) models.

https://doi.org/10.5194/egusphere-2025-2258
Preprint. Discussion started: 28 May 2025

Figures

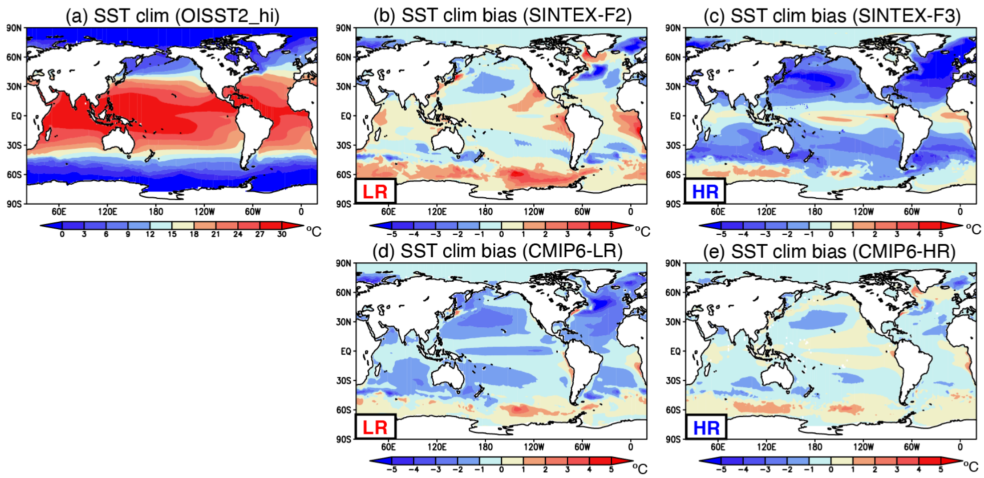

Figure 1 (a) Annual mean of the observed sea surface temperature (SST, in ºC) during 1982-2022 from the OISST2_hi dataset. **(b)** Difference in the annual mean SST (in ºC) between the SINTEX-F2 model and the OISST2_hi (i.e., model minus observation). **(c-e)** Same as in (b), but for the SINTEX-F3, CMIP6-LR, and CMIP6-HR models. The LR in the bottom left of the panel stands for the low-resolution model, whereas the HR means the high-resolution model.

https://doi.org/10.5194/egusphere-2025-2258
Preprint. Discussion started: 28 May 2025

1098 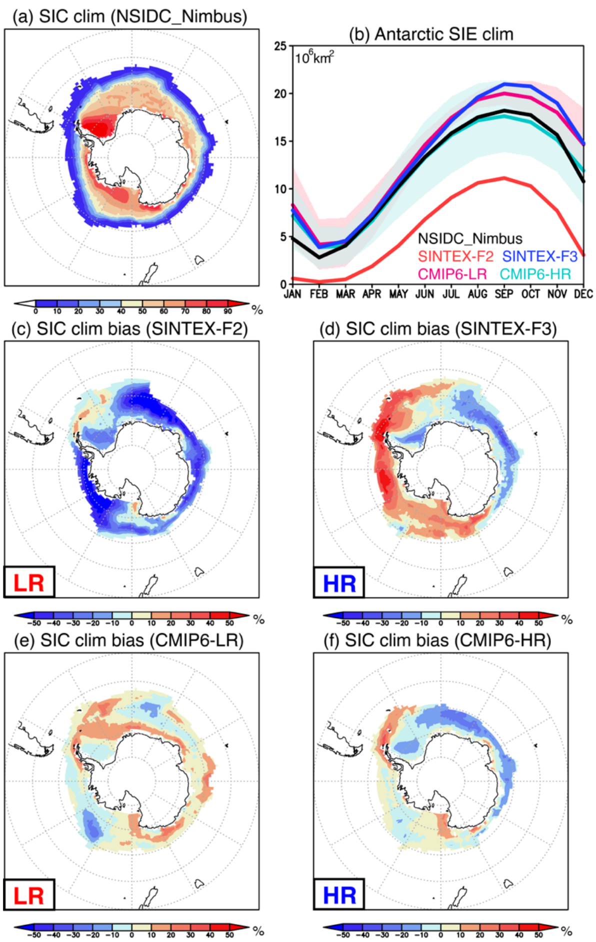

1099 **Figure 2 (a)** Annual mean of the observed sea ice concentration (SIC; in %) in the Antarctic
1100 Sea from the NSIDC_Nimbus dataset. **(b)** Monthly climatology of the Antarctic sea ice extent
1101 (SIE; in 10^6 km^2) for the NSIDC_Nimbus (black) dataset, and the SINTEX-F2 (red), SINTEX-
1102 F3 (blue), CMIP6-LR (magenta), and CMIP6-HR (light blue) models. The color shades
1103 indicate plus and minus one standard deviation of the model spreads. Here we defined the
1104 Antarctic SIE as the total area with the SIC above 15% in the Southern Hemisphere. **(c-f)**
1105 Differences in the annual mean SIC between the SINTEX-F2, SINTEX-F3, CMIP6-LR, and
1106 CMIP6-HR models and the NSIDC_Nimbus dataset (i.e., model minus observation). The LR
1107 in the bottom left of the panel stands for the low-resolution model, whereas the HR corresponds
1108 to the high-resolution model.
1109

https://doi.org/10.5194/egusphere-2025-2258
Preprint. Discussion started: 28 May 2025

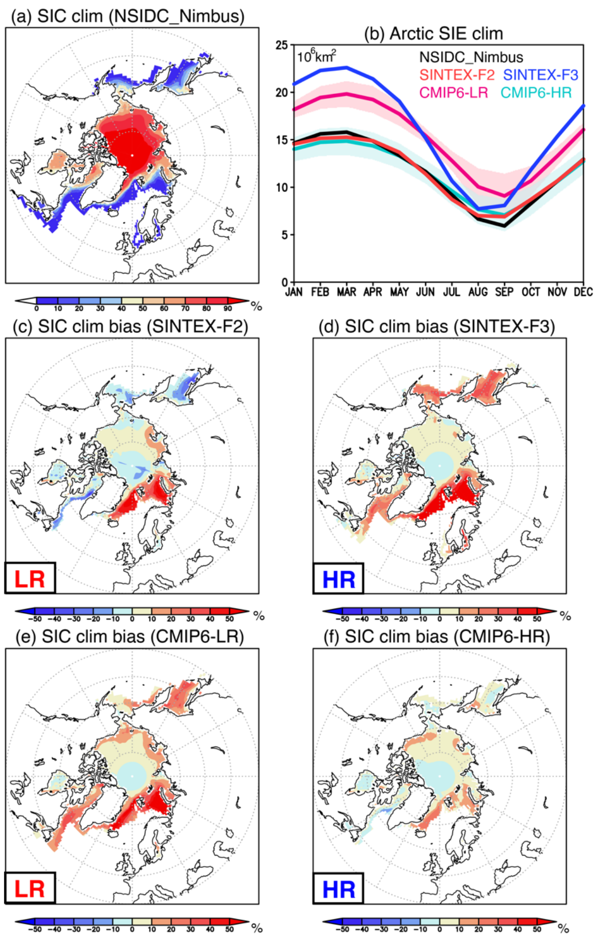

Figure 3 Same as in Fig. 2, but for the Arctic Sea. Here we defined the Arctic SIE as the total area with the SIC above 15% in the Northern Hemisphere.

https://doi.org/10.5194/egusphere-2025-2258
Preprint. Discussion started: 28 May 2025

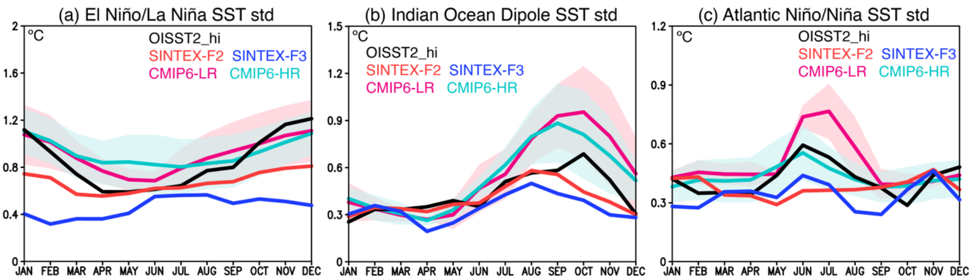

Figure 4 (a) Monthly standard deviation of the NINO3.4 index (170ºW-120ºW, 5ºS-5ºN; in ºC) for the OISST2_hi (black) dataset, and the SINTEX-F2 (red), SINTEX-F3 (blue), CMIP6-LR (magenta), and CMIP6-HR (light blue) models. The color shades indicate plus and minus one standard deviation of the model spreads. **(b-c)** Same as in (a), but for the Dipole Mode index (50ºE-70ºE, 10ºS-10ºN minus 90ºE-110ºE, 10ºS-Eq; in ºC) of the Indian Ocean Dipole and the ATL3 index (20ºW-Eq, 3ºS-3ºN; in ºC) of the Atlantic Niño/Niña.

https://doi.org/10.5194/egusphere-2025-2258
Preprint. Discussion started: 28 May 2025

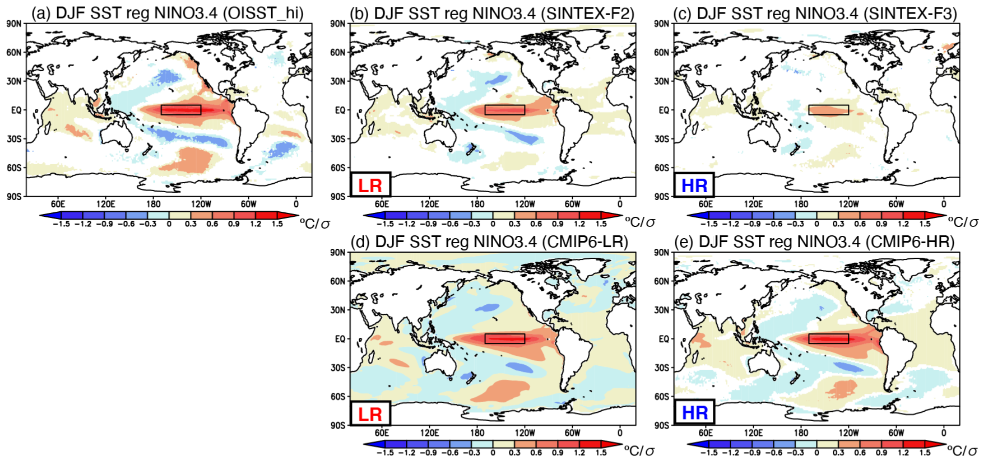

Figure 5 (a) Spatial pattern of December-February mean SST anomalies (in ºC/ σ) regressed onto the standardized NINO3.4 index for the OISST2_hi dataset. Color indicates a statistically significant value that exceeds 90 % confidence level using a Student's *t*-test. A black box indicates a region in which we calculated the NINO3.4 index. **(b-e)** Same as in (a), but for the SINTEX-F2, SINTEX-F3, CMIP6-LR, and CMIP6-HR models. The LR in the bottom left of the panel stands for the low-resolution model, whereas the HR corresponds to the high-resolution model. Note that because of the limited number of the CMIP6-LR models (i.e., 3 models), we did not apply statistical test to the regression values for the CMIP6-LR models.

https://doi.org/10.5194/egusphere-2025-2258
Preprint. Discussion started: 28 May 2025

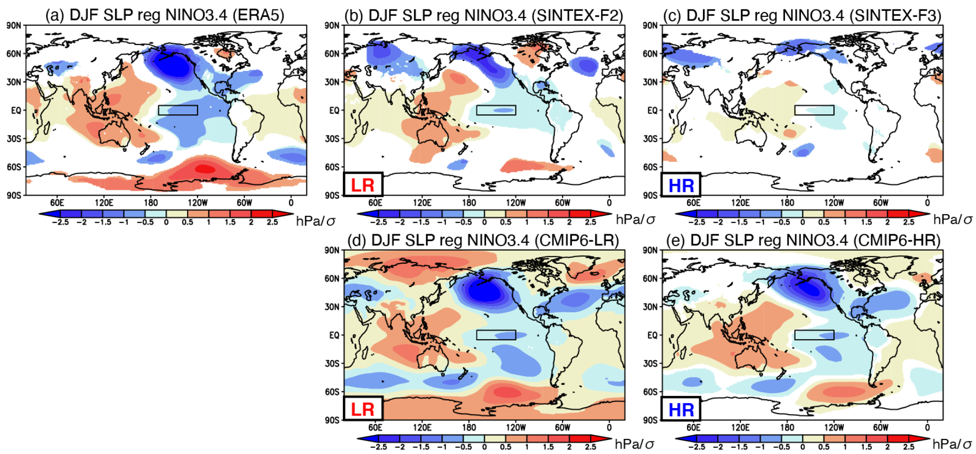

Figure 6 (a) Spatial pattern of December-February mean SLP anomalies (in hPa/ σ) regressed onto the standardized NINO3.4 index for the ERA5 reanalysis product. Color indicates a statistically significant value that exceeds 90 % confidence level using a Student's *t*-test. A black box indicates a region in which we calculated the NINO3.4 index. **(b-e)** Same as in (a), but for the SINTEX-F2, SINTEX-F3, CMIP6-LR, and CMIP6-HR models. The LR in the bottom left of the panel stands for the low-resolution model, whereas the HR corresponds to the high-resolution model. Note that because of the limited number of the CMIP6-LR models (i.e., 3 models), we did not apply statistical test to the regression values for the CMIP6-LR models.

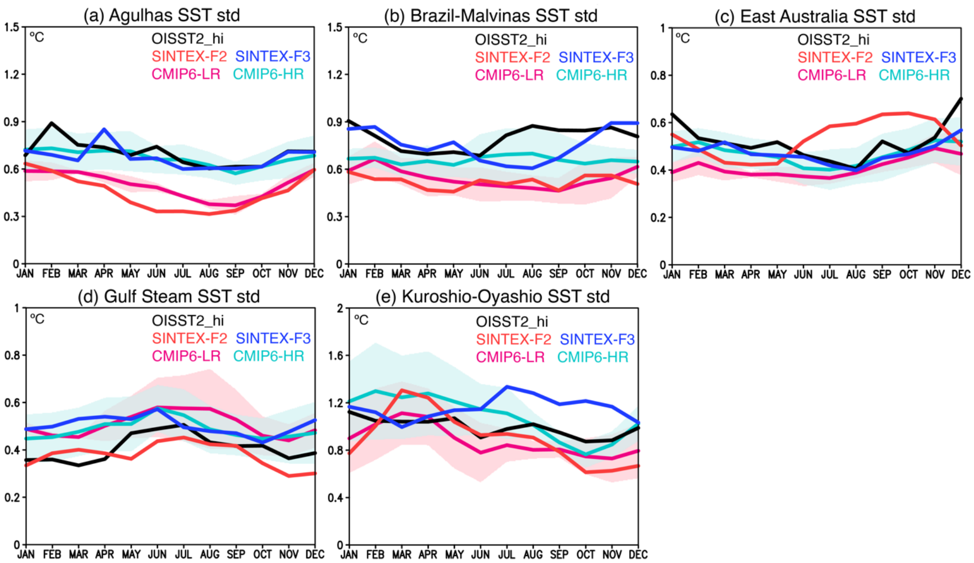

Figure 7 (a) Monthly standard deviation of the SST anomalies (in ºC) averaged over the Agulhas Retroflection Current (15ºE-30ºE, 42ºS-40ºS) region for the OISST2_hi (black) dataset, and the SINTEX-F2 (red), SINTEX-F3 (blue), CMIP6-LR (magenta), and CMIP6-HR (light blue) models. Color shades indicate plus and minus one standard deviation of the model spreads. **(b-e)** Same as in (a), but for the SST anomalies (in ºC) averaged over the Brazil-Malvinas Current (55ºW-52ºW, 45ºS-36ºS), East Australian Current (150ºE-155ºE, 40ºS-30ºS), Gulf Stream (75ºW-40ºW, 35ºN-48ºN), and Kuroshio-Oyashio (142ºE-147ºE, 36ºN-41ºN) regions.

https://doi.org/10.5194/egusphere-2025-2258
Preprint. Discussion started: 28 May 2025

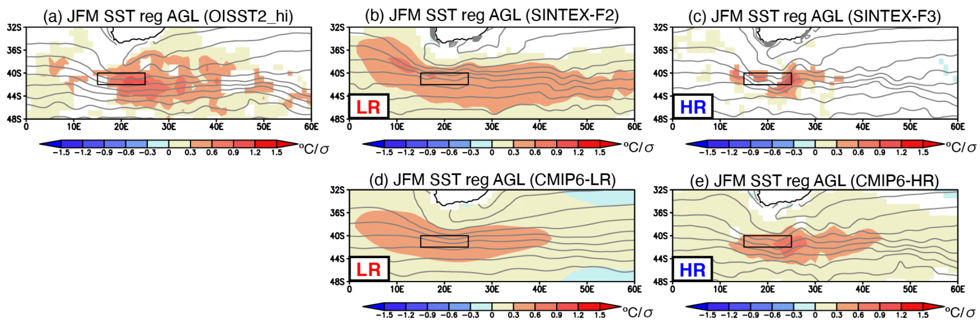

Figure 8 (a) Spatial pattern of January-March mean SST climatology (gray contour, C.I. 2 ºC) and SST anomalies (in ºC/ σ) regressed onto the standardized SST index over the Agulhas Retroflection Current (15ºE-30ºE, 42ºS-40ºS; black box) region for the OISST2_hi data. Color indicates a statistically significant value that exceeds 90 % confidence level using a Student's *t*-test. **(b-e)** Same as in (a), but for the SINTEX-F2, SINTEX-F3, CMIP6-LR, and CMIP6-HR models. The LR in the bottom left of the panel stands for the low-resolution model, whereas the HR corresponds to the high-resolution model. Note that because of the limited number of the CMIP6-LR models (i.e., 3 models), we did not apply statistical test to the regression values for the CMIP6-LR models.

https://doi.org/10.5194/egusphere-2025-2258
Preprint. Discussion started: 28 May 2025

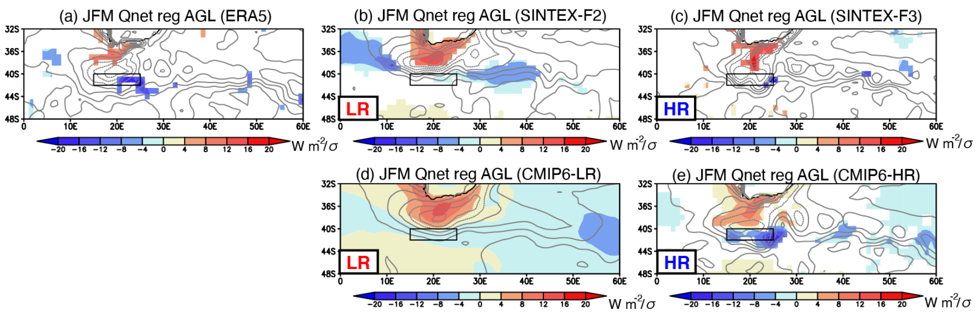

Figure 9 (a) Spatial pattern of January-March mean net surface heat flux climatology (gray contour, C.I. 30 W m^{-2}/ σ) and net surface heat flux anomalies (in W m^{-2}/ σ) regressed onto the standardized SST index over the Agulhas Retroflection Current (15ºE-30ºE, 42ºS-40ºS; black box) region for the ERA5 reanalysis product. Color indicates a statistically significant value that exceeds 80 % confidence level using a Student's *t*-test. Positive surface heat flux values indicate the heat going into the ocean. **(b-e)** Same as in (a), but for the SINTEX-F2, SINTEX-F3, CMIP6-LR, and CMIP6-HR models. The LR in the bottom left of the panel stands for the low-resolution model, whereas the HR corresponds to the high-resolution model. Note that because of the limited number of the CMIP6-LR models (i.e., 3 models), we did not apply statistical test to the regression values for the CMIP6-LR models.

https://doi.org/10.5194/egusphere-2025-2258
Preprint. Discussion started: 28 May 2025

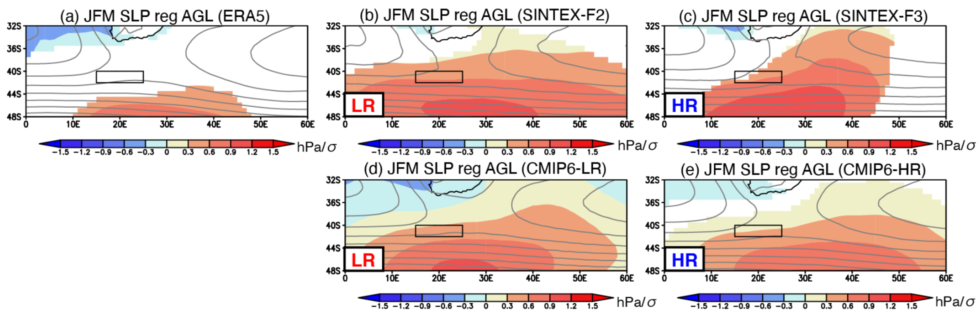

Figure 10 (a) Spatial pattern of January-March mean SLP climatology (gray contour, C.I. 2 hPa) and SLP anomalies (in hPa/ σ) regressed onto the standardized SST index over the Agulhas Retroflection Current (15ºE-30ºE, 42ºS-40ºS; black box) region for the ERA5 reanalysis product. Color indicates a statistically significant value that exceeds 90 % confidence level using a Student's *t*-test. **(b-e)** Same as in (a), but for the SINTEX-F2, SINTEX-F3, CMIP6-LR, and CMIP6-HR models. The LR in the bottom left of the panel stands for the low-resolution model, whereas the HR corresponds to the high-resolution model. Note that because of the limited number of the CMIP6-LR models (i.e., 3 models), we did not apply statistical test to the regression values for the CMIP6-LR models.

https://doi.org/10.5194/egusphere-2025-2258
Preprint. Discussion started: 28 May 2025

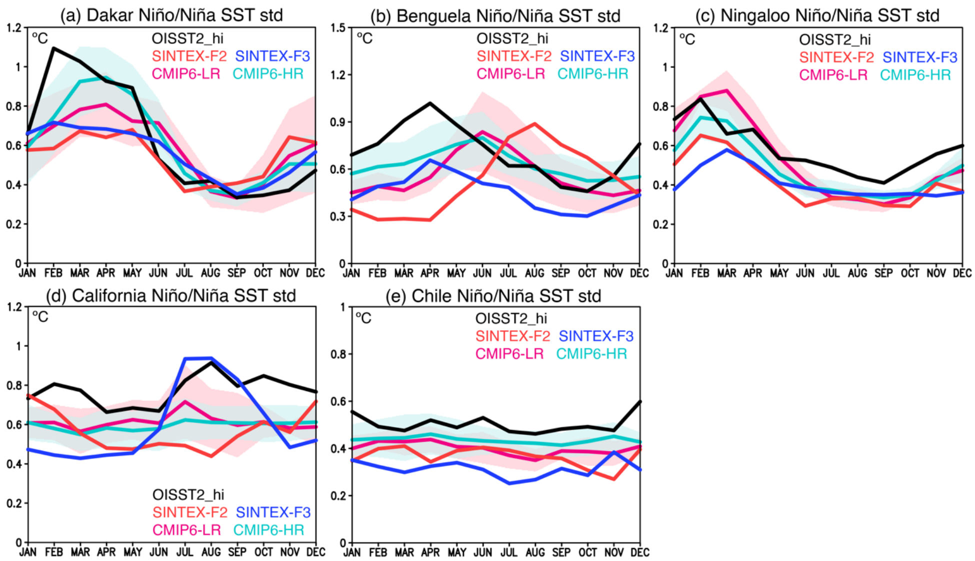

1187

1188 **Figure 11 (a)** Monthly standard deviation of the SST anomalies (in ºC) averaged over the
1189 Dakar Niño/Niña (21ºW-17ºW, 9ºN-14ºN) region for the OISST2_hi (black) dataset, and the
1190 SINTEX-F2 (red), SINTEX-F3 (blue), CMIP6-LR (magenta), and CMIP6-HR (light blue)
1191 models. Color shades indicate plus and minus one standard deviation of the model spreads. **(b-**
1192 **e)** Same as in (a), but for the SST anomalies (in ºC) averaged over the Benguela Niño/Niña
1193 (8ºE-14ºE, 20ºS-10ºS), Ningaloo Niño/Niña (108ºE-115ºE, 28ºS-22ºS), California Niño/Niña
1194 (120ºW-130ºW, 20ºN-30ºN), and Chile Niño/Niña (80ºW-70ºW, 35ºS-20ºS) regions.

1195

https://doi.org/10.5194/egusphere-2025-2258
Preprint. Discussion started: 28 May 2025

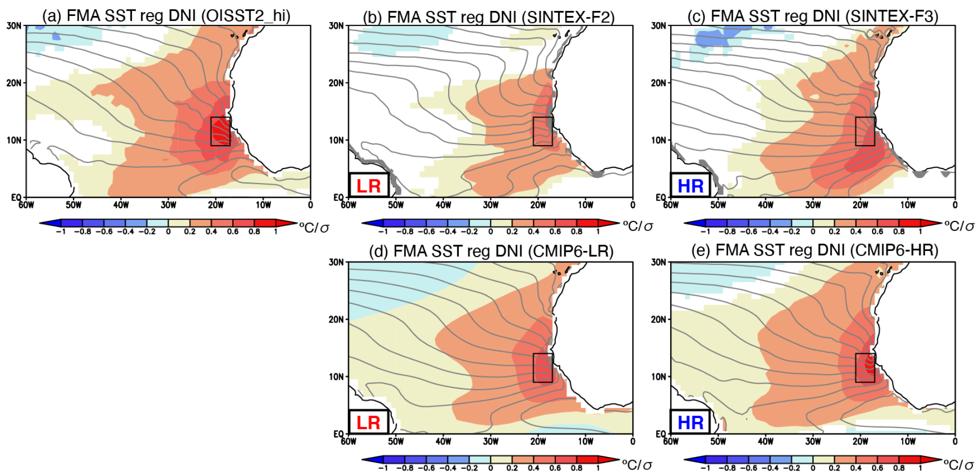

Figure 12 (a) Spatial pattern of February-April mean SST climatology (gray contour, C.I. 1 ºC) and SST anomalies (in ºC/ σ) regressed onto the standardized Dakar Niño/Niña SST index (DNI; 21ºW-17ºW, 9ºN-14ºN in a black box) for the OISST2_hi data. Color indicates a statistically significant value that exceeds 90 % confidence level using a Student's *t*-test. **(b-e)** Same as in (a), but for the SINTEX-F2, SINTEX-F3, CMIP6-LR, and CMIP6-HR models. The LR in the bottom left of the panel stands for the low-resolution model, whereas the HR corresponds to the high-resolution model. Note that because of the limited number of the CMIP6-LR models (i.e., 3 models), we did not apply statistical test to the regression values for the CMIP6-LR models.

https://doi.org/10.5194/egusphere-2025-2258
Preprint. Discussion started: 28 May 2025

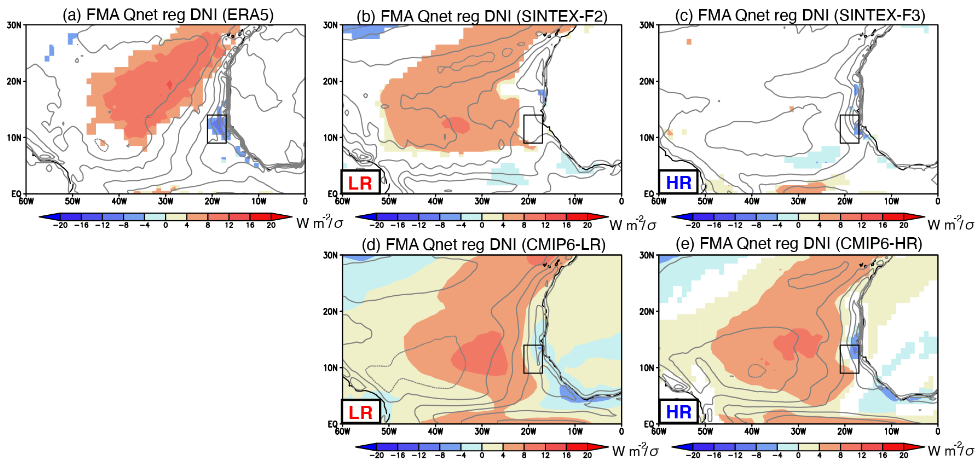

Figure 13 (a) Spatial pattern of February-April mean net surface heat flux climatology (gray contour, C.I. 20 W m^{-2}/ σ) and net surface heat flux anomalies (in W m^{-2}/ σ) regressed onto the standardized Dakar Niño/Niña SST index (DNI; 21ºW-17ºW, 9ºN-14ºN in a black box) for the ERA5 reanalysis product. Color indicates a statistically significant value that exceeds 80 % confidence level using a Student's *t*-test. Positive surface heat flux values indicate the heat going into the ocean. **(b-e)** Same as in (a), but for the SINTEX-F2, SINTEX-F3, CMIP6-LR, and CMIP6-HR models. The LR in the bottom left of the panel stands for the low-resolution model, whereas the HR corresponds to the high-resolution model. Note that because of the limited number of the CMIP6-LR models (i.e., 3 models), we did not apply statistical test to the regression values for the CMIP6-LR models.

https://doi.org/10.5194/egusphere-2025-2258
Preprint. Discussion started: 28 May 2025

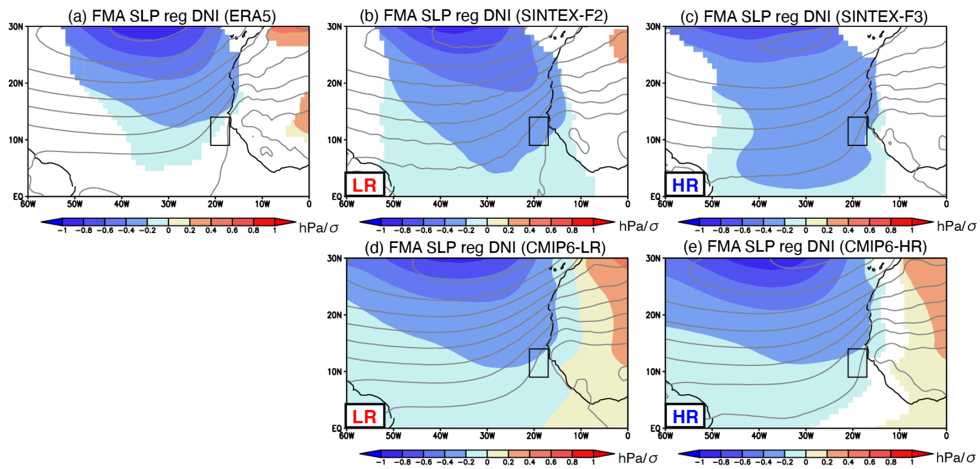

Figure 14 (a) Spatial pattern of February-April mean SLP climatology (gray contour, C.I. 1.5 hPa) and SLP anomalies (in hPa/ σ) regressed onto the standardized Dakar Niño/Niña SST index (DNI; 21ºW-17ºW, 9ºN-14ºN in a black box) for the ERA5 reanalysis product. Color indicates a statistically significant value that exceeds 90 % confidence level using a Student's *t*-test. **(b-e)** Same as in (a), but for the SINTEX-F2, SINTEX-F3, CMIP6-LR, and CMIP6-HR models. The LR in the bottom left of the panel stands for the low-resolution model, whereas the HR corresponds to the high-resolution model. Note that because of the limited number of the CMIP6-LR models (i.e., 3 models), we did not apply statistical test to the regression values for the CMIP6-LR models.

https://doi.org/10.5194/egusphere-2025-2258
Preprint. Discussion started: 28 May 2025

1230 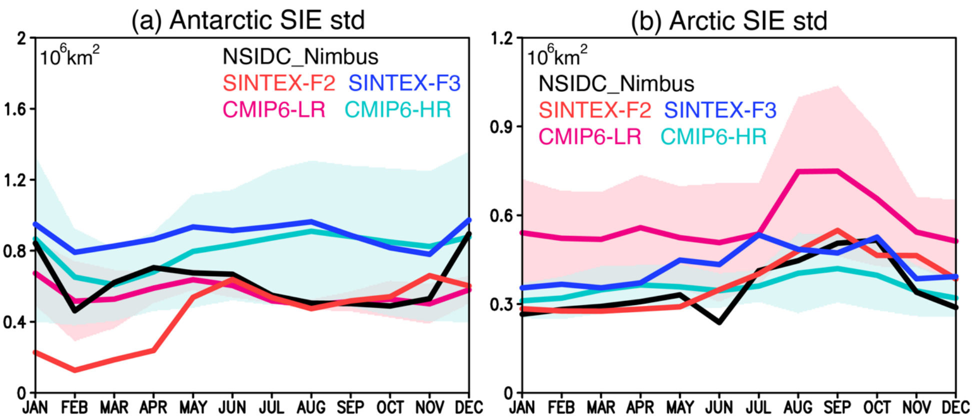

1231 **Figure 15 (a)** Monthly standard deviation of Antarctic sea ice extent (SIE; in 10^6 km^2) for the
1232 NSIDC_Nimbus (black) dataset, and the SINTEX-F2 (red), SINTEX-F3 (blue), CMIP6-LR
1233 (magenta), and CMIP6-HR (light blue) models. Color shades indicate plus and minus one
1234 standard deviation of the model spreads. **(b)** Same as in (a), but for the the Arctic SIE.

1235

https://doi.org/10.5194/egusphere-2025-2258
Preprint. Discussion started: 28 May 2025

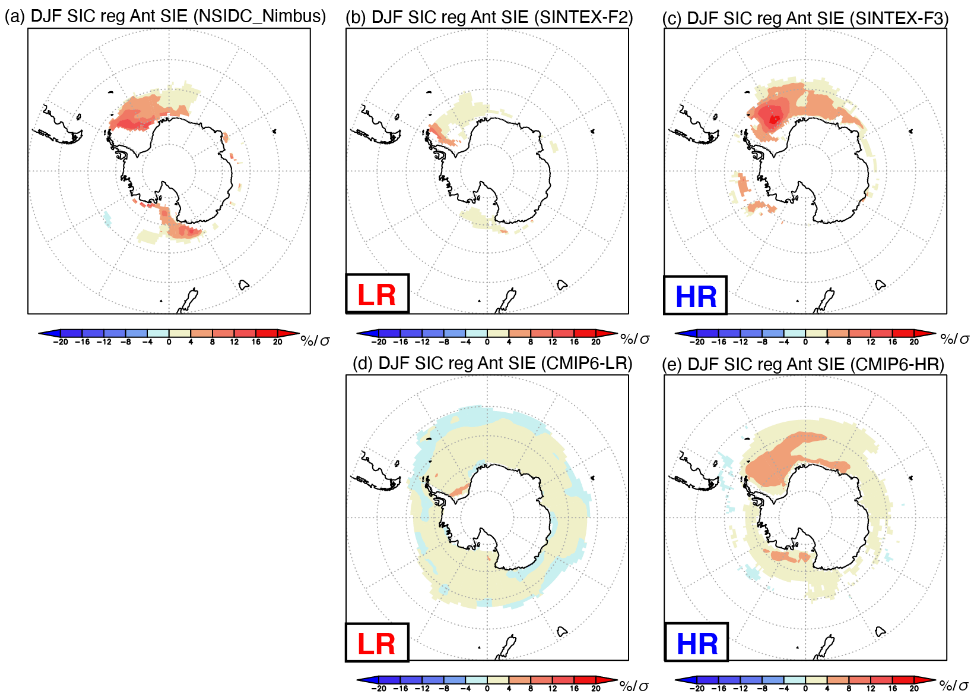

Figure 16 (a) Spatial pattern of December-February mean sea ice concentration anomalies (SIC; in %/ σ) regressed onto the standardized Antarctic sea ice extent (SIE) anomalies for the NSIDC_Nimbus dataset. Color indicates a statistically significant value that exceeds 90 % confidence level using a Student's *t*-test. **(b-e)** Same as in (a), but for the SINTEX-F2, SINTEX-F3, CMIP6-LR, and CMIP6-HR models. The LR in the bottom left of the panel stands for the low-resolution model, whereas the HR corresponds to the high-resolution model. Note that because of the limited number of the CMIP6-LR models (i.e., 3 models), we did not apply statistical test to the regression values for the CMIP6-LR models.

https://doi.org/10.5194/egusphere-2025-2258
Preprint. Discussion started: 28 May 2025

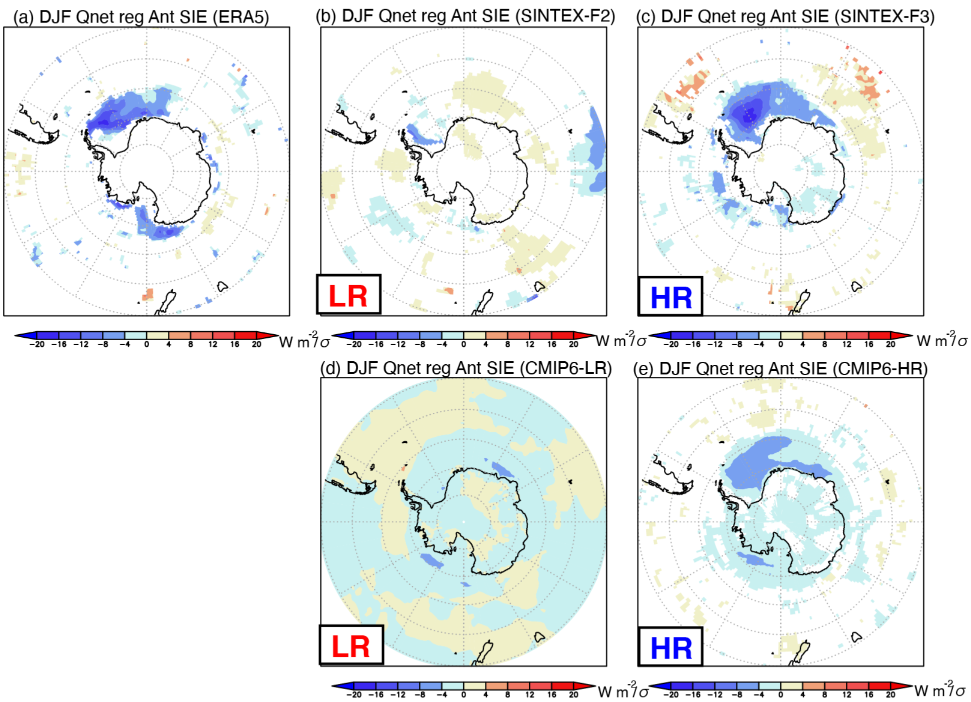

1246

1247 **Figure 17 (a)** Spatial pattern of December-February mean net surface heat flux anomalies (in
1248 W m^{-2}/ σ) regressed onto the standardized Antarctic sea ice extent (SIE) anomalies for the
1249 ERA5 reanalysis. Color indicates a statistically significant value that exceeds 80% confidence
1250 level using a Student's *t*-test. **(b-e)** Same as in (a), but for the SINTEX-F2, SINTEX-F3,
1251 CMIP6-LR, and CMIP6-HR models. The LR in the bottom left of the panel stands for the low-
1252 resolution model, whereas the HR corresponds to the high-resolution model. Note that because
1253 of the limited number of the CMIP6-LR models (i.e., 3 models), we did not apply statistical
1254 test to the regression values for the CMIP6-LR models.

1255

https://doi.org/10.5194/egusphere-2025-2258
Preprint. Discussion started: 28 May 2025

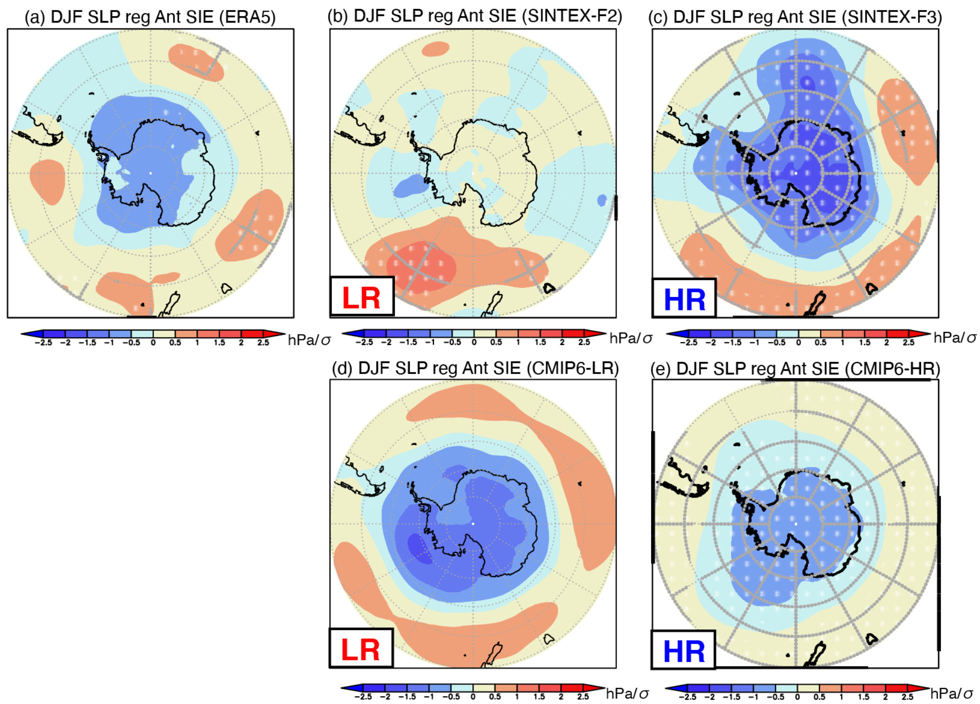

Figure 18 (a) Spatial pattern of December-February mean sea level pressure anomalies (SLP; in hPa/ σ) regressed onto the standardized Antarctic sea ice extent (SIE) anomalies for the ERA5 reanalysis. A white dot indicates a statistically significant value that exceeds 90 % confidence level using a Student's *t*-test. **(b-e)** Same as in (a), but for the SINTEX-F2, SINTEX-F3, CMIP6-LR, and CMIP6-HR models. The LR in the bottom left of the panel stands for the low-resolution model, whereas the HR corresponds to the high-resolution model. Note that because of the limited number of the CMIP6-LR models (i.e., 3 models), we did not apply statistical test to the regression values for the CMIP6-LR models.